ANALYSIS OF EX-VESSEL STEAM EXPLOSIONS FOR THE COMBUSTION ENGINEERING SYSTEM 80+ USING THE *GT3F*™ COMPUTER CODE

JUNE 1994

79 pp

CONTENTS

1 Introduction

This document presents the results of a study of ex-vessel steam explosions for the Combustion Engineering System 80+ reactors. The computer code $GT3F^{TM}$ [1, 2] was utilized for modeling molten fuel-water interaction in the reactor cavity following a hypothetical cormelt accident. Fuel water interactions resulting from the following three separate scenarios were simulated:

1. a central instrument tube rupture
2. an outer instrument tube rupture
3. multiple instrument tube ruptures

Relevant characteristics of the Combustion Engineering System 80+, and the rationale for the selection of the aforementioned scenarios can be found in [3].

In what follows, the steam explosion following the failure of the central instrument tube is first addressed in Section 2, followed in Section 3 by the results of the analysis of a steam explosion resulting from an outer instrument tube failure. The case of multiple instrument tube rupture is discussed in Section 4. Recommendations for future work are presented in Section 5.

It is well recognized that fragmentation of the molten fuel during the propagation phase of a steam explosion is a key process which strongly affects the course of the transient. Details of the relevant fragmentation models incorporated in the $GT3F^{TM}$ computer code [1, 2] are provided in Appendix A.

Prior to the application of $GT3F^{TM}$ to the Combustion Engineering System 80+ scenarios, the code was benchmarked against Test # 21 of KROTOS steam explosion

experiments [19]. Furthermore, in accordance with the method reported in [1, 2], an empirical constant, namely, the limiting Weber number, in the molten fuel fragmentation model of $GT3F^{TM}$ was adjusted in order to match the model-predicted and experimentally- measured pressure peaks in the aforementioned KROTOS test. Details of this benchmarking are provided in Appendix B.

2 Central Instrument Tube Failure

The system configuration is depicted in Figure 2.1. At the initiation of tube failure, a single Corium jet, 3 cm in diameter, was assumed to flow downward into the water with a velocity of 5.5 m/s. The initial water pool temperature was assumed to be 393 K, and the pressure was assumed to be 2 bars.

2.1 Premixing

The computational domain, depicted in Figure 2.2, was nodalized using 10 radial nodes with $\Delta r = 3$ cm, and 27 axial nodes with $\Delta z = 20$ cm. It was not necessary to model the entire 1.5 m radius region during premixing since no changes were anticipated outside the selected computation domain. In the analysis, a lower limit of $DP = 10$ mm was assumed for melt particle diameter. The time step was 100 μs. Premixing calculations were performed for a total of 2 seconds.

The calculated results at various times during the premixing phase of the explosion are depicted in the following attached figures.

Figure 2.3: Molten fuel volume fraction contours

Figure 2.4: Void fraction (gas phase volume fraction) contours

Figure 2.5: Pressure contours

2.2 Triggering and Propagation

The computational domain for the triggering, propagation, and expansion phases of the steam explosion following a central instrument tube failure is depicted in Figure 2.6. The calculations were performed using 27 axial nodes with $\Delta z = 20$ cm, and 50 radial nodes with $\Delta r = 3$ cm. The time step size was 2 μs. The explosion was assumed to be triggered at one second after the initiation of premixing. Triggering was assumed to take place on the axis of symmetry of the jet, 4.1 m above the bottom of the liquid pool which corresponds to the mid plane elevation of the submerged portion of the corbel supports. Triggering was simulated in the code by assuming that, at the triggering time, 10% of the molten fuel in node (1,21) underwent complete fragmentation in one time step (2 μs). The critical Weber number for the initiation of molten fuel fragmentation was assumed to be 100.

The calculated results are depicted in the following attached figures.

Figure 2.7: Molten Fuel volume fraction contours

Figure 2.8: Void fraction (gas phase volume fraction) contours

Figure 2.9: Pressure contours

Figure 2.10: Pressure histories at various nodes

In order to examine the effect of nodalization on the predicted results, the above triggering and propagation calculations were repeated, this time using 25 radial nodes

with $\Delta r = 6$ cm. All other parameter were maintained unchanged. Pressure histories at various nodes for this calculation are presented in Figure 2.11. A comparison between Figures 2.10 and 2.11 indicates that the node size can affect the computed results. For example, as noted, the predicted peak pressures are considerably higher for the smaller radial node size.

The calculated pressure impulse distributions over the corbel support surface are depicted in Figure 2.12. These values were determined by integrating the pressure histories at various axial locations along the wall. The maximum impulse is approximately 10.5 kPa.s, and occurs at the bottom elevation of the corbel support (axial node 18). The pressure impulse monotonically decreases with height, and reaches a minimum value of approximately 5.5 kPa.s at axial node 27, representing the water level height before the initiation of the transient. These predicted pressure impulse loads are significantly lower than the 5th percentile impulse capacity for corbel supports, which is approximately 35 kPa.s [3]. The decreasing impulse with height is consistent with the predictions of TEXAS and IFCI codes [3]. The pressure impulses predicted by the TEXAS code are significantly higher, however, and are in the 12 to 42 kPa.s range [3]. The IFCI code, on the other hand, predicts pressure impulses in the 3 to 15 kPa.s over the corbel surface [3], and is in good agreement with $GT3F^{TM}$ predictions. The results shown in Figures 2.12 also indicate that reducing the radial node size from $\Delta r = 6$ cm to $\Delta r = 3$ cm had a slight effect on the predicted pressure impulse distributions.

3 Outer Instrument Tube Failure

The system configuration is shown in Figure 3.1. The axis of the molten fuel jet resulting from the failure of the outer instrument tube was assumed to be 15 cm away from the corbel support wall. The jet was assumed to be 3 cm in diameter, and the melt jet velocity, calculated based on the molten Corium hydrostatic head in the vessel lower head above the jet exit, was assumed to be 4.6 m/s. The water pool was initially at 393 K temperature and 2 bar pressure.

3.1 Premixing

The computational domain used to perform the premixing calculation is depicted in Figure 3.2. In order to render two-dimensional calculations in polar cylindrical coordinates possible, the computational domain was chosen to be a cylinder 15 cm in diameter, with its centerline coincident with the centerline of the molten fuel jet. The computational domain was nodalized using 5 radial nodes with $\Delta r = 3$ cm, and 27 axial nodes with $\Delta z = 20$ cm. The time step was 100 μs. A lower limit of $DP = 10$ mm was assumed for melt particles. Premixing calculations were performed for a total period of 2 seconds.

The calculated results are depicted in the following attached figures.

Figure 3.3: Molten fuel volume fraction contours

Figure 3.4: Void fraction (gas phase volume fraction) contours

Figure 3.5: Pressure contours

3.2 Triggering and Propagation

These calculations were performed using the aforementioned computational domain and nodalization scheme for the premixing calculations (Figure 3.2). Thus, 27 axial nodes with $\Delta z = 20$ cm, and 5 radial nodes with $\Delta r = 3$ cm were used. The time step size was 2 μs. The explosion was assumed to be triggered at one second after the initiation of premixing. The critical Weber number for the initiation of molten fuel fragmentation was assumed to be 100. Triggering was assumed to take place on the axis of symmetry of the molten fuel jet, 4.1 m above the bottom of the liquid pool in node (1,21) which corresponds to the mid plane elevation of the submerged portion of the corbel supports. The explosion was assumed to be triggered one second after initiation of premixing. Triggering was simulated in the code by assuming that, at the time of triggering, 10% of the molten fuel in node (1,21) underwent complete fragmentation in one time step (2 μs).

The calculated results are depicted in the following attached figures.

Figure 3.6: Molten fuel volume fraction contours

Figure 3.7: Void fraction (gas phase volume fraction) contours

Figure 3.8: Pressure contours

Figure 3.9: Pressure histories at various nodes

Figure 3.10 Pressure impulse distribution over the corbel support surface

It should be noted that the impulse values calculated for this transient are significantly higher than those for the central instrument tube failure. It is also significantly higher

than the 5th percentile impulse capacity for the corbel supports. These results are not surprising in view of the proximity of the jet to the corbel supports wall.

4 Multiple Instrument Tube Failure

The system configuration is depicted in Figure 4.1. Eight similar holes, each 3 cm in diameter, and supporting molten fuel jets with a velocity of 5.5 m/s, were assumed to simultaneously form due to the failure of the eight instrument tubes nearest to the vessel centerline. The water pool was assumed to be initially at 393 K temperature and 2 bar pressure.

4.1 Premixing

The computational domain used to perform the premixing calculations is depicted in Figure 4.2. Calculations were performed using 10 radial nodes with $\Delta r = 15$ cm, and 27 axial nodes with $\Delta z = 20$ cm. A lower limit of $DP = 10$ mm was assumed for melt particles. The time step was 100 μs. In order to make a two-dimensional analysis in polar cylindrical coordinates possible, and in accordance with the physical location of the failed tubes, the molten jets were distributed over the radial nodes as follows:

Radial node # 1 (centerline)	1 jet
Radial node # 2	1.5 jets
Radial node # 3	1.5 jets
Radial node # 4	2 jets
Radial node # 5	2 jets

Consistent with the two-dimensional (r,z) nodalization scheme, the molten jets

arriving at each radial node are uniformly distributed over the node cross-sectional area. This clearly leads to low concentrations of molten fuel in the system due to the applied coarse radial mesh, as well as the two dimensional nature of the simulation.

The calculated results are depicted in the following attached figures.

Figure 4.3: Molten fuel volume fraction contours

Figure 4.4: Void fraction (gas phase volume fraction) contours

Figure 4.5: Pressure contours

As noted, the calculated molten fuel concentrations are extremely low (less that 2%) everywhere in the computational zone, and throughout the premixing phase. Such low concentrations of molten fuel are evidently unrealistic, and do not provide the necessary conditions for a steam explosion resulting in significant pressure peaks. The predicted low molten fuel concentrations are due to the two-dimensional (r,z) simulation of an essentially three-dimensional process, along with the application of a coarse radial mesh.

4.2 Triggering and Propagation

These calculations were performed using the aforementioned computational domain and nodalization scheme for the premixing calculations (Figure 4.2). Thus, 27 axial nodes with $\Delta z = 20$ cm, and 10 radial nodes with $\Delta r = 15$ cm were used. The time step size was 2 μs. The explosion was assumed to be triggered at one second after the initiation of premixing. The critical Weber number for the initiation of molten fuel fragmentation was assumed to be 100. Triggering was simulated in the code

by assuming that, at the time of triggering, 10% of the molten fuel in node (1,21) underwent complete fragmentation in one time step (2 μs). Again, this corresponds to the mid plane elevation of the submerged portion of the corbel supports.

The calculated results for 7.5 ms are depicted in the following attached figures.

Figure 4.6: Molten fuel volume fraction contours

Figure 4.7: Void fraction (gas phase volume fraction) contours

Figure 4.8: Pressure contours

Figure 4.9: Pressure impulse distribution over the corbel support surface

As noted, the predicted pressures are quite low, and result in an unreasonably low pressure impulse distribution. These results, which indicate a lower pressure impulse than the case with a single jet due to the rupture of a central instrument tube (see Section 2), are questionable. The reason, as mentioned in the previous subsection, is the two-dimensional (r,z) simulation, along with the application of coarse radial nodes. The applied nodalization scheme distributes the incoming fuel jets over the cross-sectional areas of large radial nodes, and smears the high molten fuel concentration explosion zones.

5 Recommendations for Future Work

- The triggering and propagation calculations for central and outer instrument tube failure cases (Sections 2 and 3) were performed in this work assuming that triggering occurred on the centerline of the melt jet at 4.1 m above the

bottom of the water pool, one second after the initiation of premixing. It is recommended that triggering and propagation calculations be repeated assuming that triggering occurs at the bottom of the pool upon impact of the molten fuel.

- The two-dimensional (r,z) modeling of premixing, as well as triggering and propagation phases of the steam explosion resulting from multiple instrument tube failure leads to unrealistic predictions. It is recommended that these calculations be repeated using a significantly finer radial mesh.

- The multiple tube failure steam explosion is essentially a three-dimensional process, and a two-dimensional (r,z) simulation, even with fine radial mesh, may not be adequate for its analysis. A three-dimensional (r, θ, z) analysis, in which a reasonably small slice of the system (e.g.,$\Delta\theta = 45^0$) is simulated, is recommended.

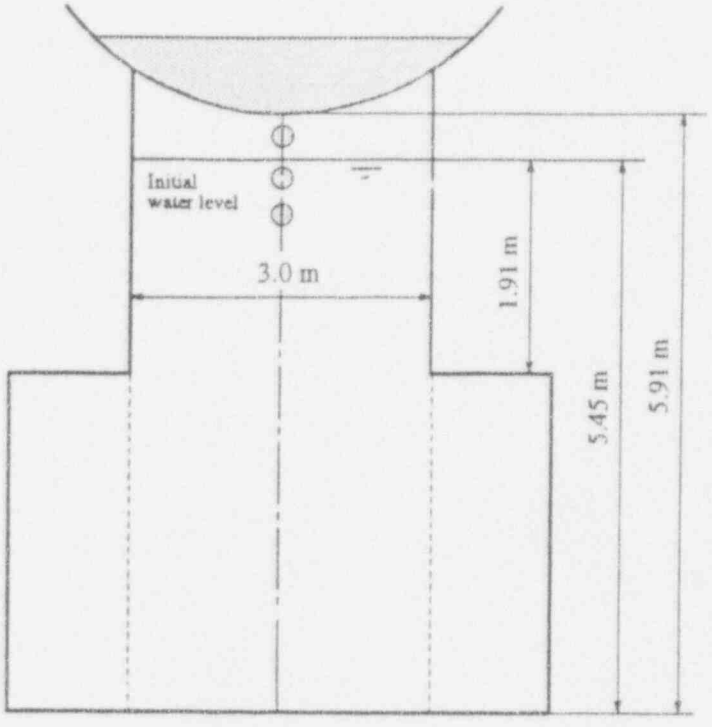

Figure 2.1: Overall Configuration for Central Instrument Tube Failure

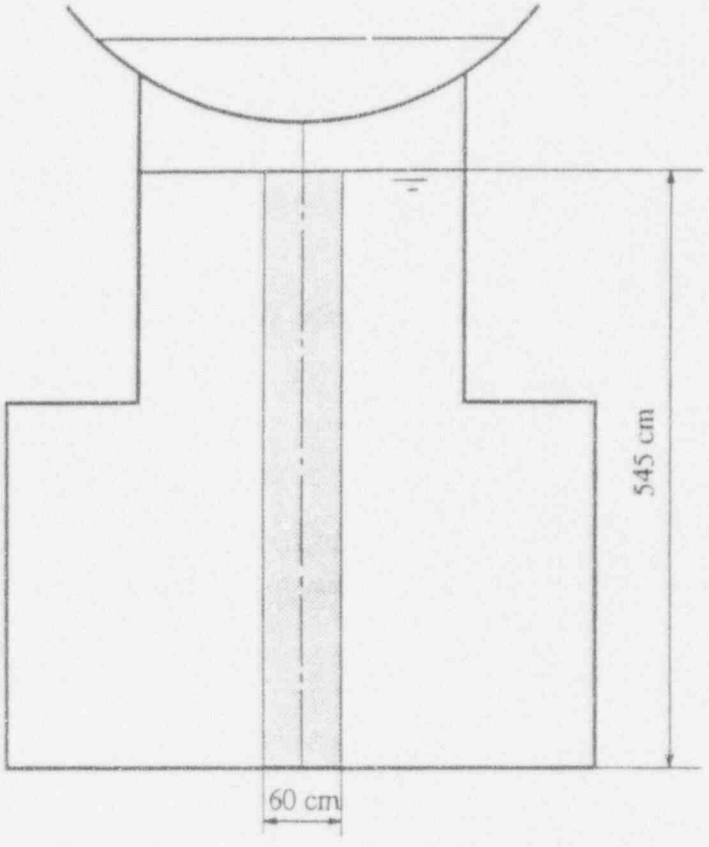

Figure 2.2: Central Instrument Tube Failure
(Shaded area represents computational domain for premixing calculation)

Figure 2.3
Central Instrument Tube Failure–Premixing
Fuel Volume Fraction
(Δr = 3.0 cm, Δz = 20.0 cm)

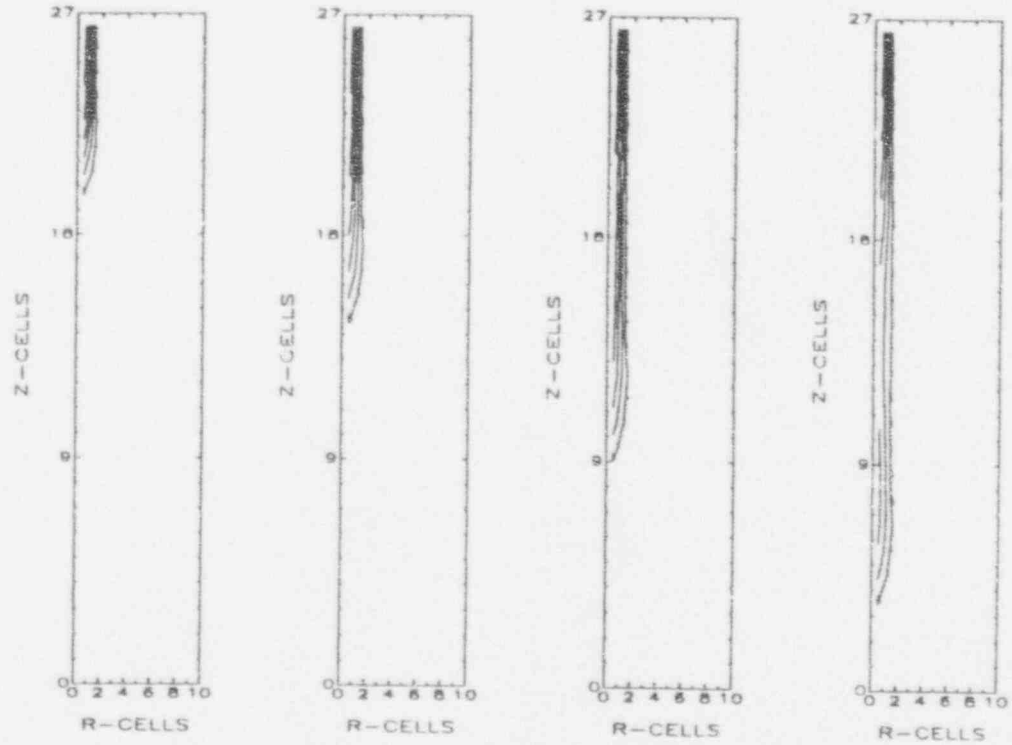

0.25 sec	0.50 sec	0.75 sec	1.00 sec
H=0.2231	H=0.2343	H=0.2345	H=0.2420
L=0.0000	L=0.0000	L=0.0000	L=0.0000

Figure 2.3 (contd)
Central Instrument Tube Failure–Premixing
Fuel Volume Fraction
($\Delta r = 3.0$ cm, $\Delta z = 20.0$ cm)

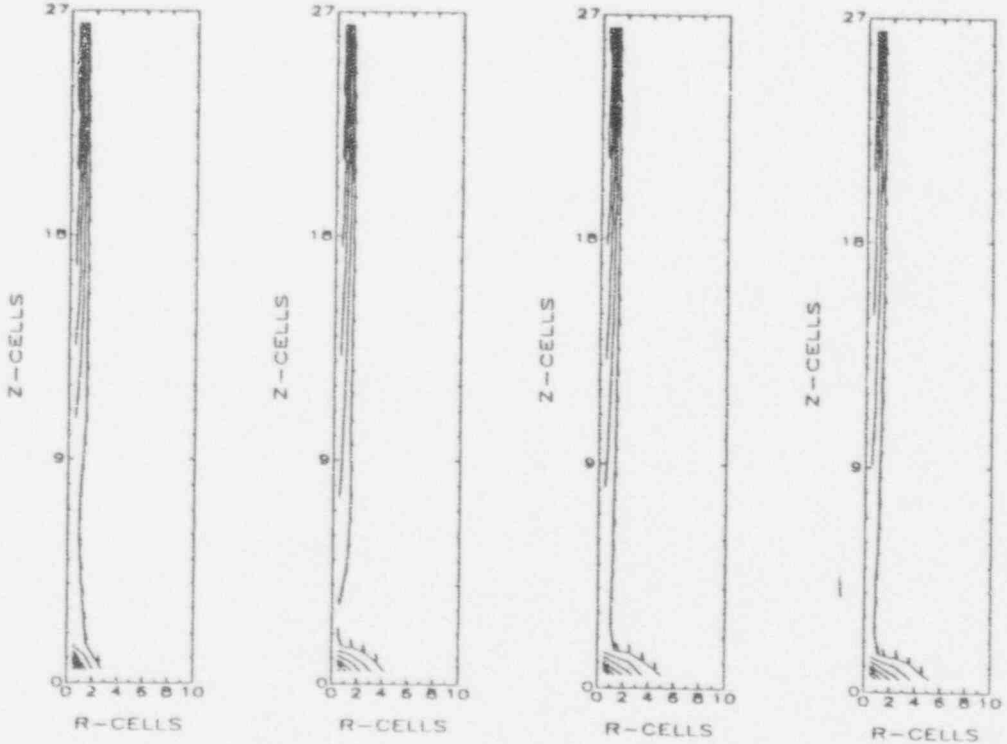

1.25 sec
H=0.2341
L=0.0000

1.50 sec
H=0.2423
L=0.0000

1.75 sec
H=0.2595
L=0.0000

2.00 sec
H=0.3368
L=0.0000

Figure 2.4
Central Instrument Tube Failure–Premixing
Void Fraction
($\Delta r = 3.0$ cm, $\Delta z = 20.0$ cm)

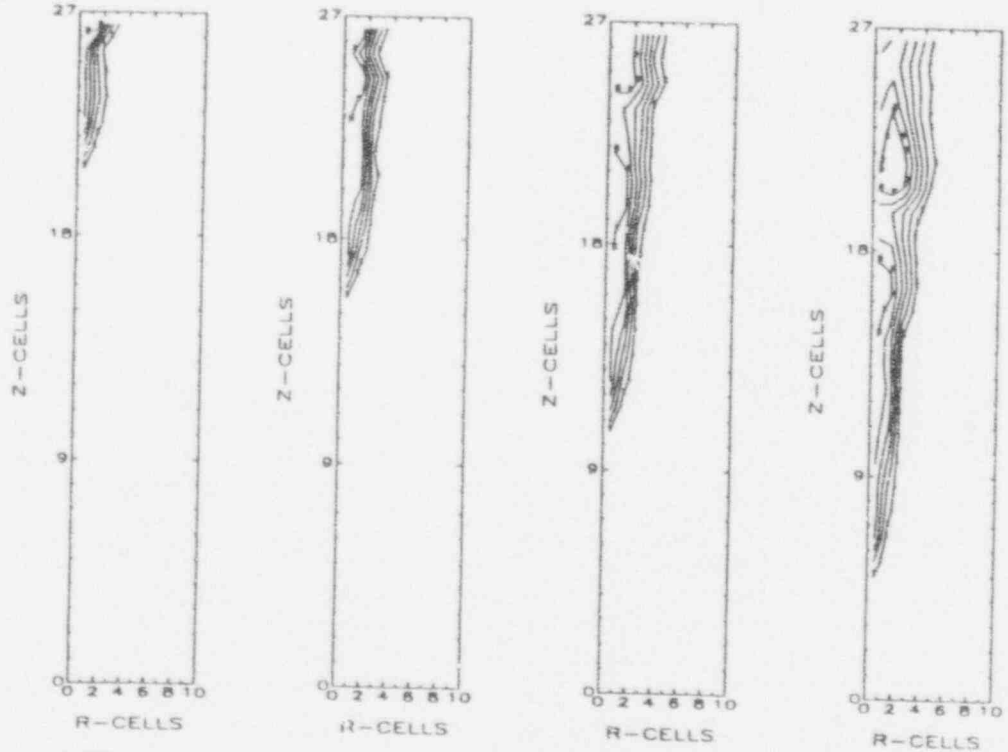

0.25 sec
H=0.8405
L=0.0000

0.50 sec
H=0.8027
L=0.0000

0.75 sec
H=0.8713
L=0.0000

1.00 sec
H= 0.9481
L=0.0000

Figure 2.4 (contd)
Central Instrument Tube Failure–Premixing
Void Fraction
(Δr = 3.0 cm, Δz = 20.0 cm)

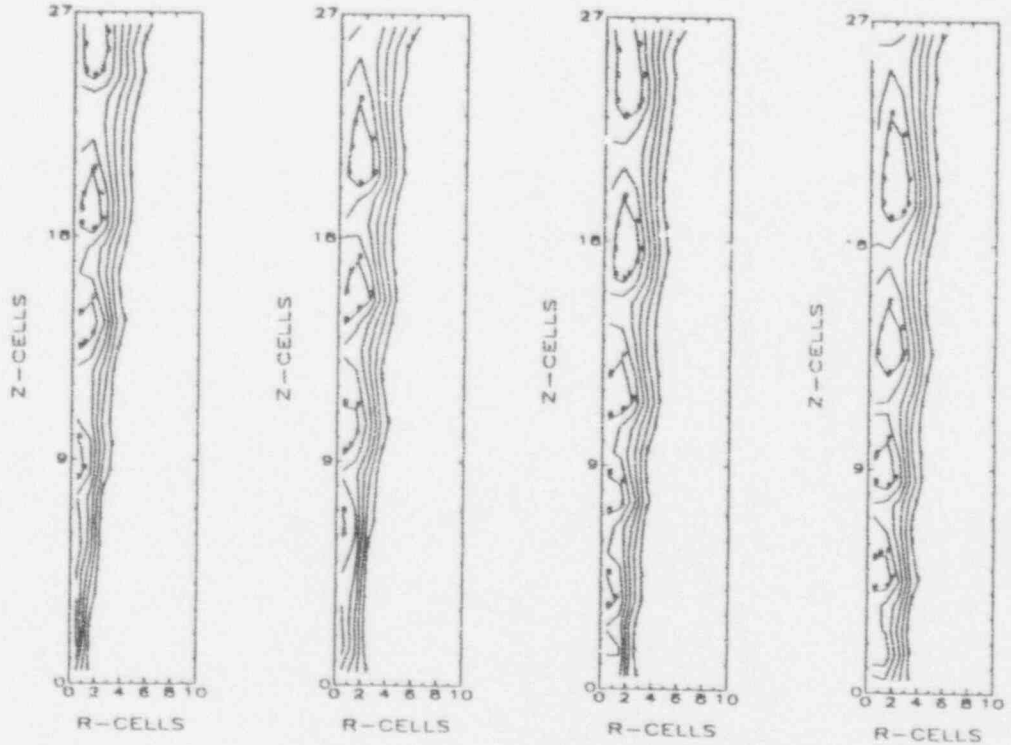

1.25 sec
H=0.9202
L=0.0000

1.50 sec
H=0.9185
L=0.0000

1.75 sec
H=0.9048
L=0.0000

2.00 sec
H=0.9046
L=0.0000

Figure 2.5
Central Instrument Tube Failure–Premixing
Pressure (bar)
(Δr = 3.0 cm, Δz = 20.0 cm)

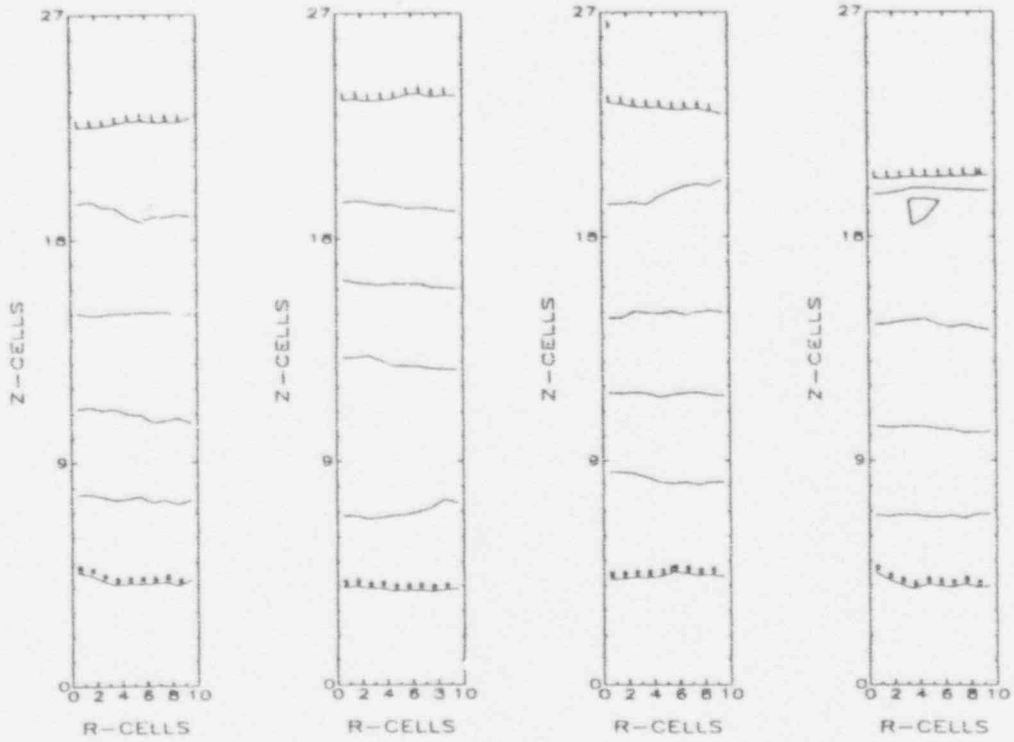

0.25 sec	0.50 sec	0.75 sec	1.00 sec
H=2.529	H=2.493	H=2.498	H=2.527
L=2.004	L=2.010	L=1.998	L=2.011

Figure 2.5 (contd)
Central Instrument Tube Failure–Premixing
Pressure (bar)
(Δr = 3.0 cm, Δz = 20.0 cm)

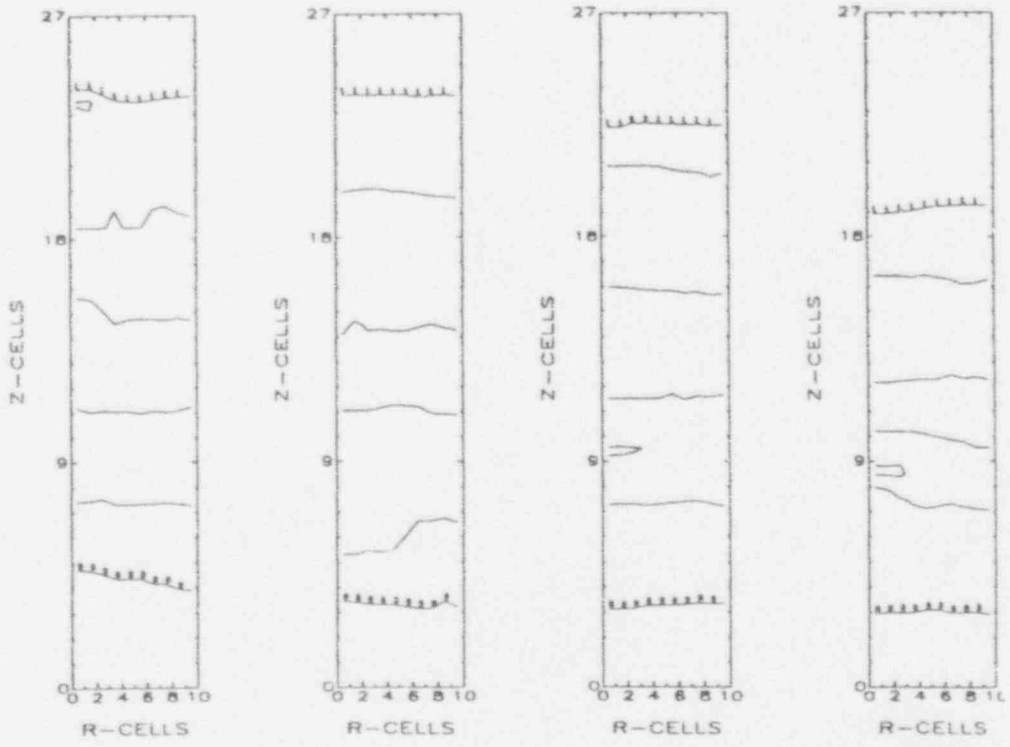

1.25 sec	1.50 sec	1.75 sec	2.00 sec
H=2.519	H=2.527	H=2.501	H=2.505
L=1.988	L=2.020	L=1.990	L=2.088

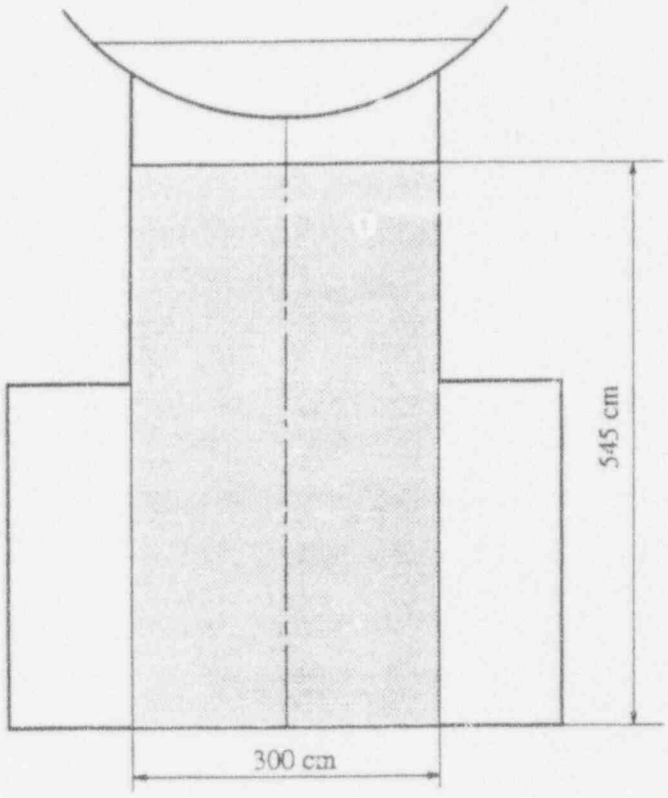

Figure 2.6: Central Instrument Tube Failure
(Shaded area represents computational domain for propagation calculation)

Figure 2.7
Central Instrument Tube Failure–Propagation
Fuel Volume Fraction
(Δr = 3.0 cm, Δz = 20.0 cm)

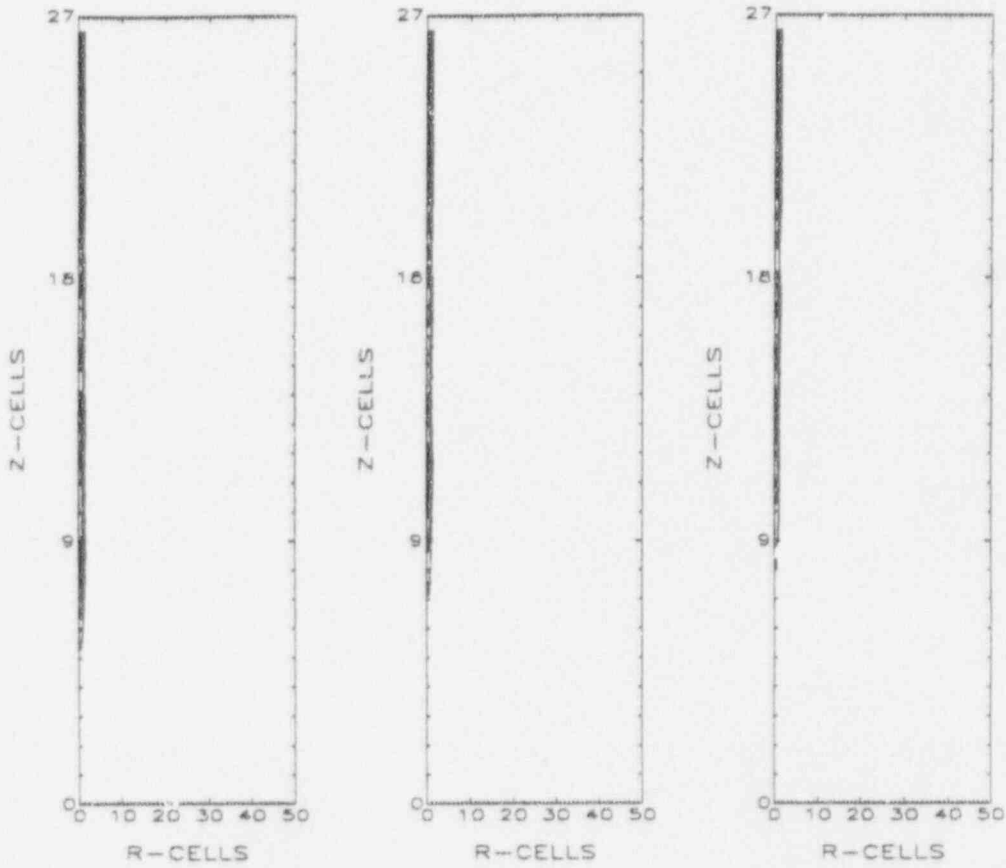

2.5 ms
H=0.2411
L=0.0000

5.0 ms
H=0.2376
L=0.0000

7.5 ms
H=0.2354
L=0.0000

Figure 2.7 (contd)
Central Instrument Tube Failure–Propagation
Fuel Volume Fraction
(Δr = 3.0 cm, Δz = 20.0 cm)

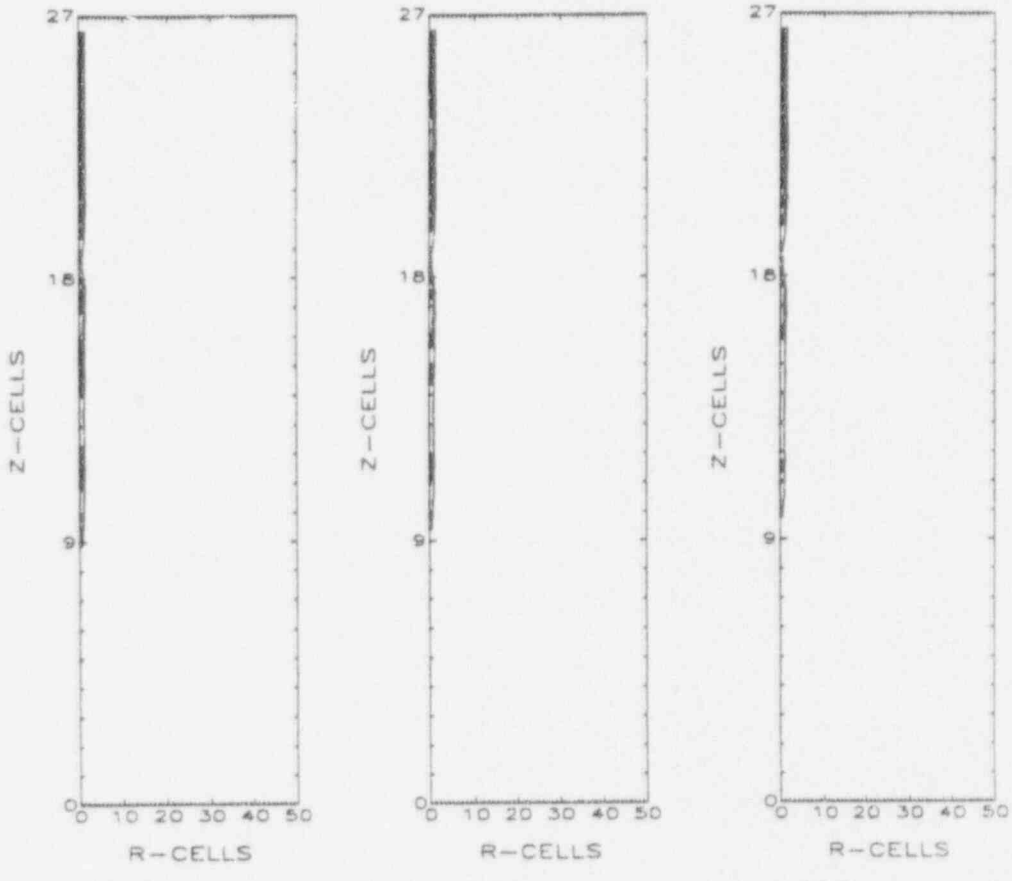

10.0 ms
H=0.2292
L=0.0000

12.5 ms
H=0.2218
L=0.0000

15.0 sec
H=0.2228
L=0.0000

Figure 2.8
Central Instrument Tube Failure–Propagation
Void Fraction
(Δr = 3.0 cm, Δz = 20.0 cm)

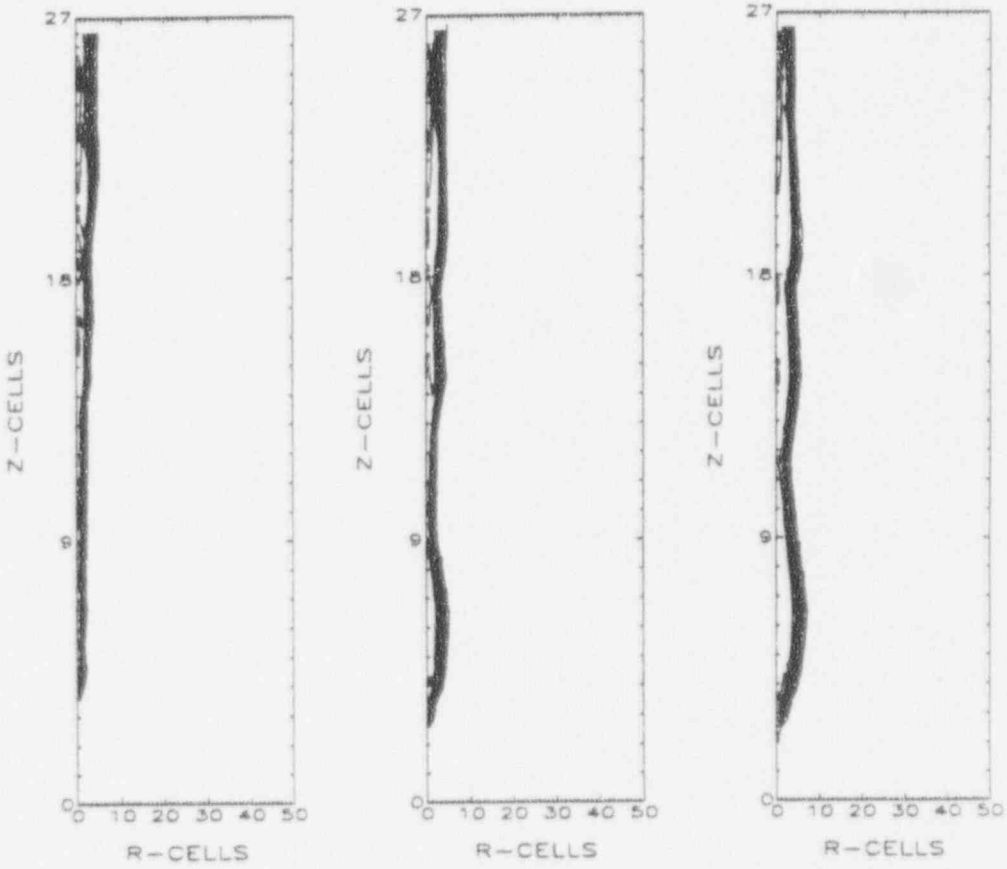

2.5 ms
H=0.9493
L=0.0000

5.0 ms
H=0.9837
L=0.0000

7.5 ms
H=0.9973
L=0.0000

Figure 2.8 (contd)
Central Instrument Tube Failure–Propagation
Void Fraction
($\Delta r = 3.0$ cm, $\Delta z = 20.0$ cm)

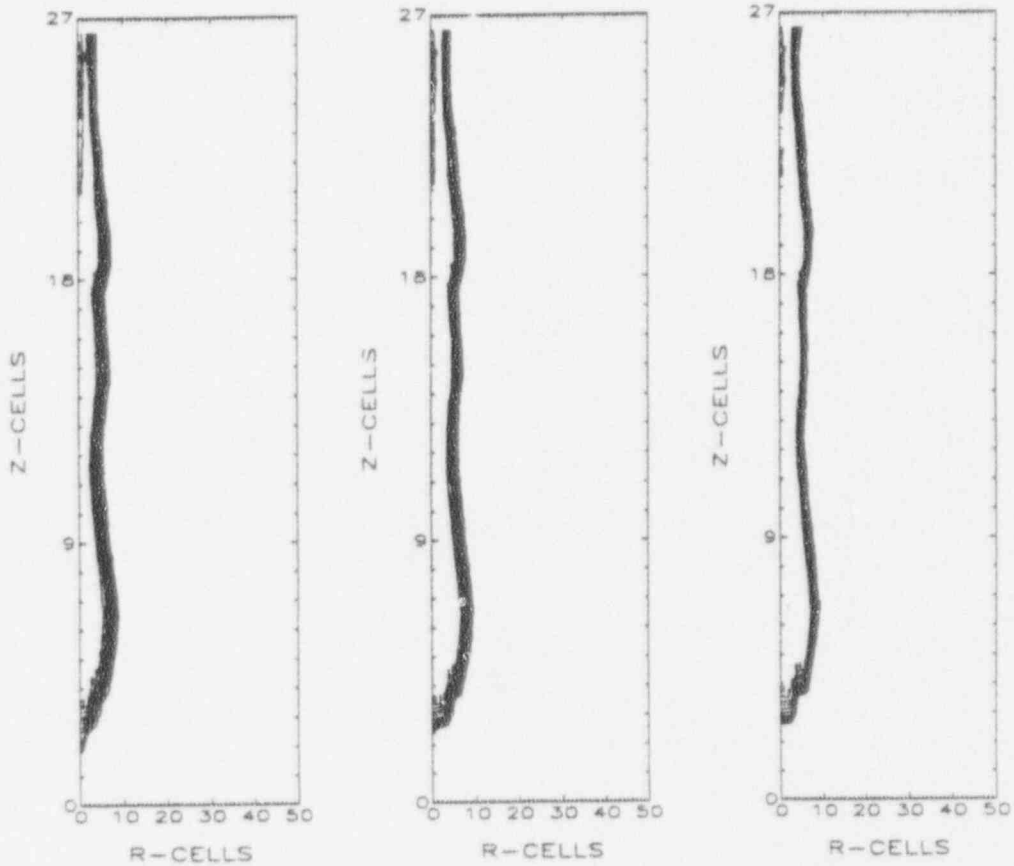

10.0 ms
H=0.9987
L=0.0000

12.5 ms
H=0.9992
L=0.0000

15.0 sec
H=0.9986
L=0.0000

Figure 2.9
Central Instrument Tube Failure–Propagation
Pressure (bar)
(Δr = 3.0 cm, Δz = 20.0 cm)

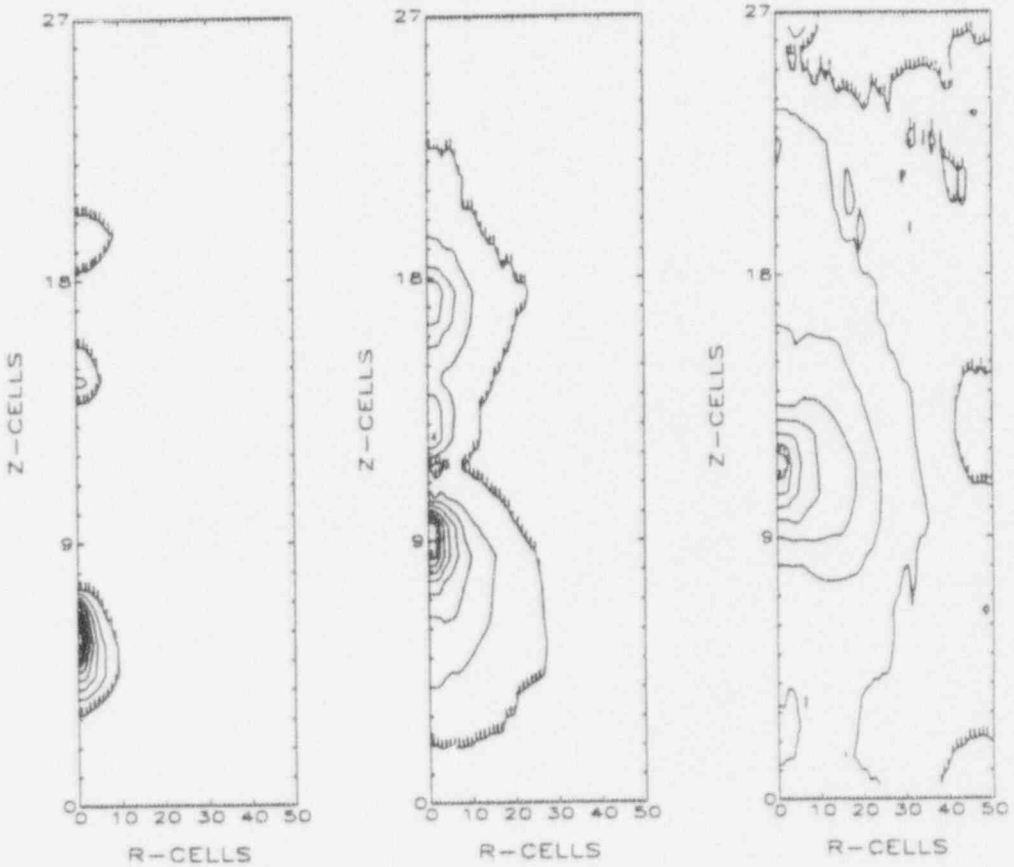

2.5 ms
H=39.98
L=2.030

5.0 ms
H=33.89
L=2.030

7.5 ms
H=20.65
L=2.285

Figure 2.9 (contd)
Central Instrument Tube Failure–Propagation
Pressure (bar)
(Δr = 3.0 cm, Δz = 20.0 cm)

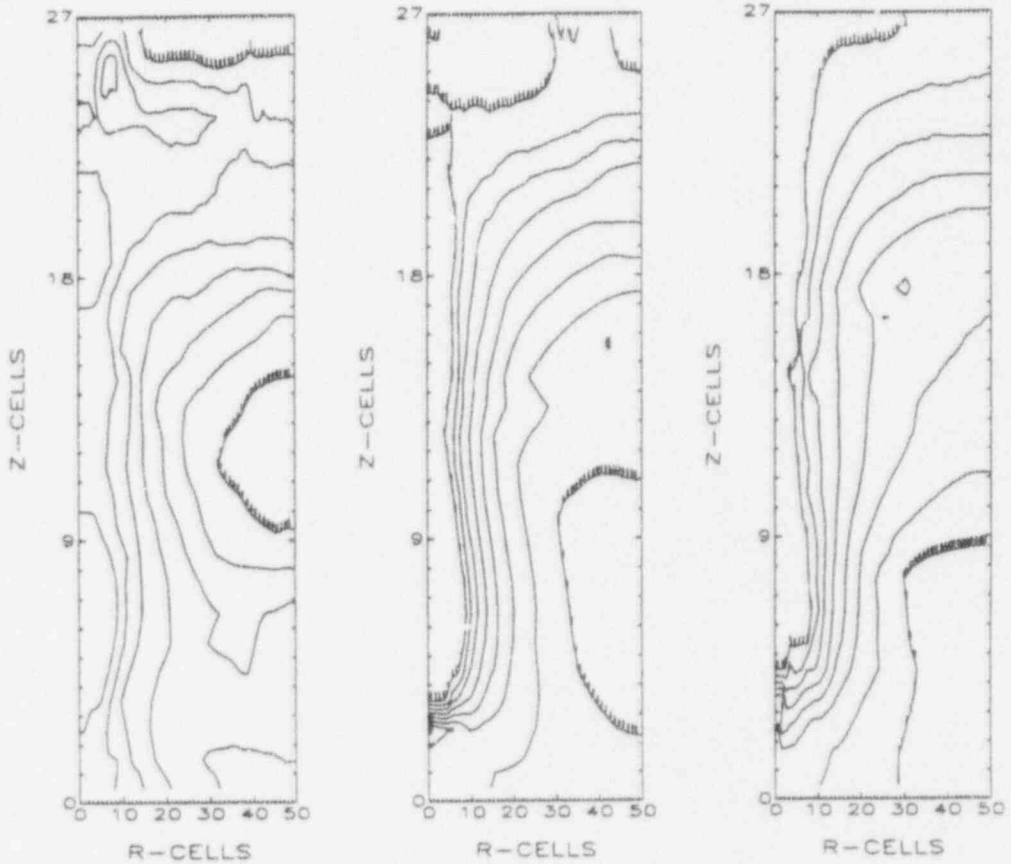

10.0 ms
H=15.76
L=2.565

12.5 ms
H=14.58
L=3.851

15.0 sec
H=14.24
L=4.006

Figure 2.10
Central Instrument Tube Failure–Propagation
Pressure (bar)
(Δr = 3.0 cm, Δz = 20.0 cm)

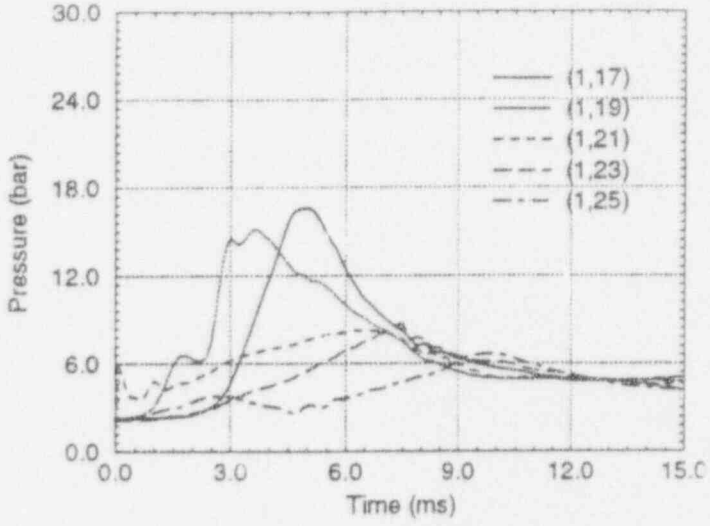

(a) Pressures along melt jet center line

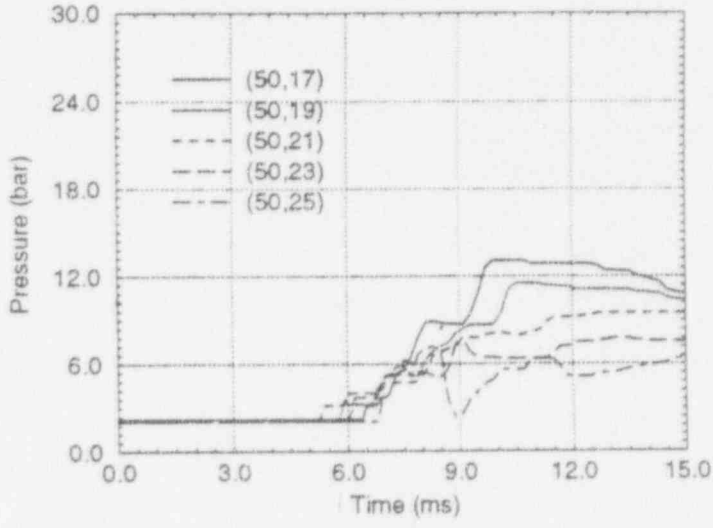

(b) Pressures along corbel support

Figure 2.11
Central Instrument Tube Failure–Propagation
Pressure (bar)
(Δr = 6.0 cm, Δz = 20.0 cm)

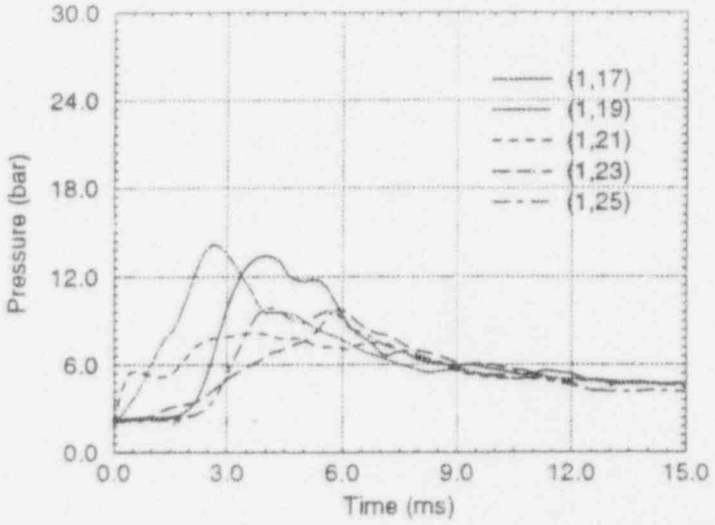

(a) Pressures along melt jet center line

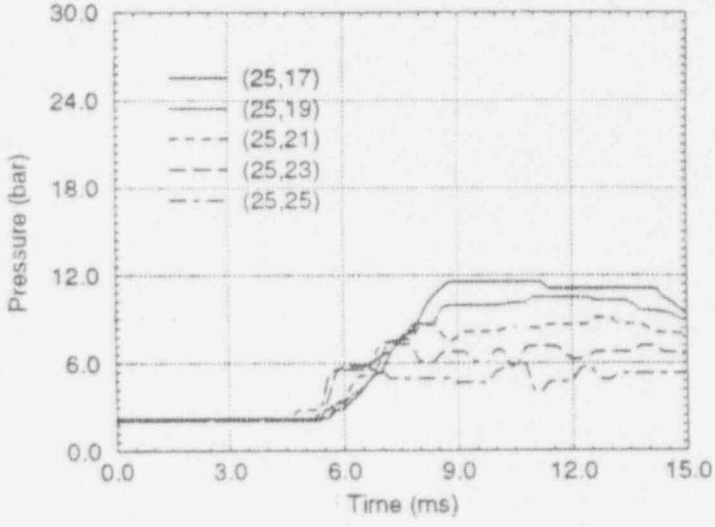

(b) Pressures along corbel support

Figure 2.12
Central Instrument Tube Failure
Impulse Distribution Along Corbel Support
(Δz = 20.0 cm)

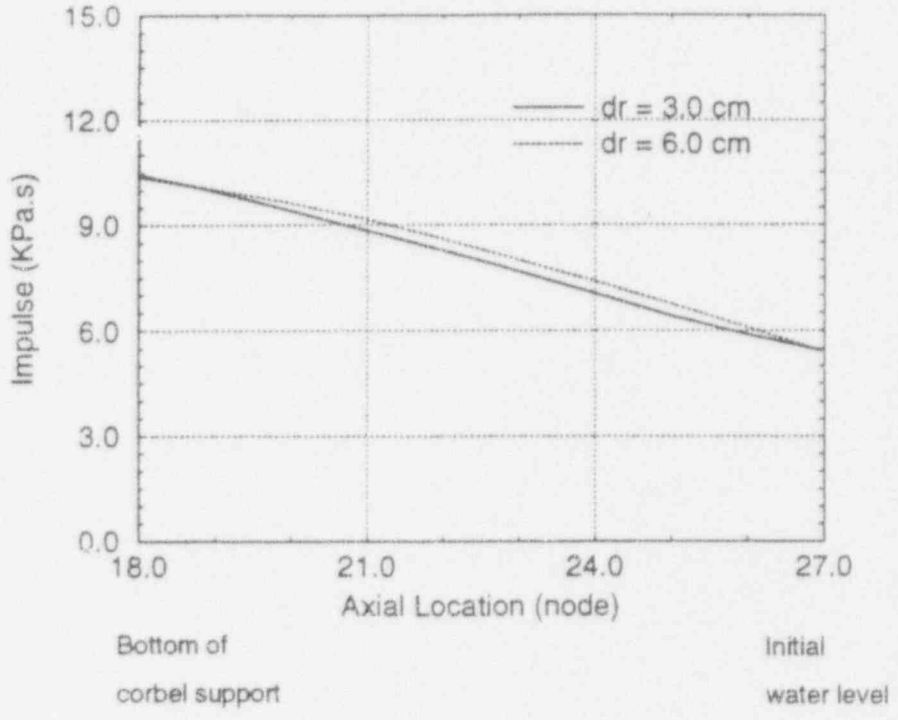

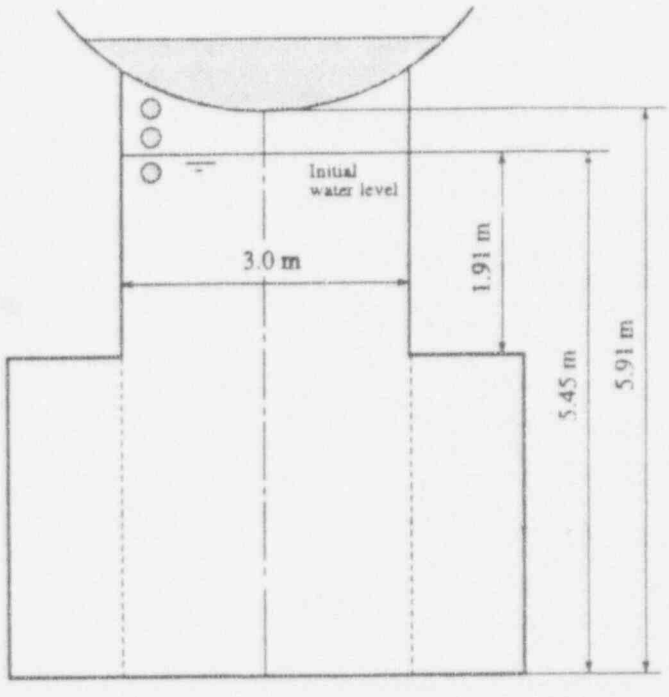

Figure 3.1: Overall Configuration for Outer Instrument Tube Failure

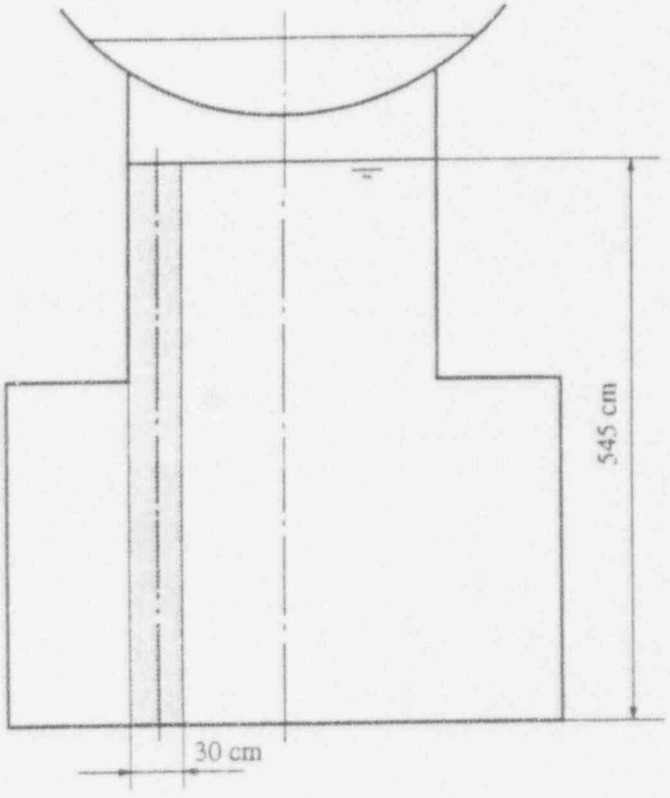

Figure 3.2: Outer Instrument Tube Failure
(Shaded area represents computational domain
for premixing and propagation calculations)

Figure 3.3
Outer Instrument Tube Failure–Premixing
Fuel Volume Fraction
($\Delta r = 3.0$ cm, $\Delta z = 20.0$ cm)

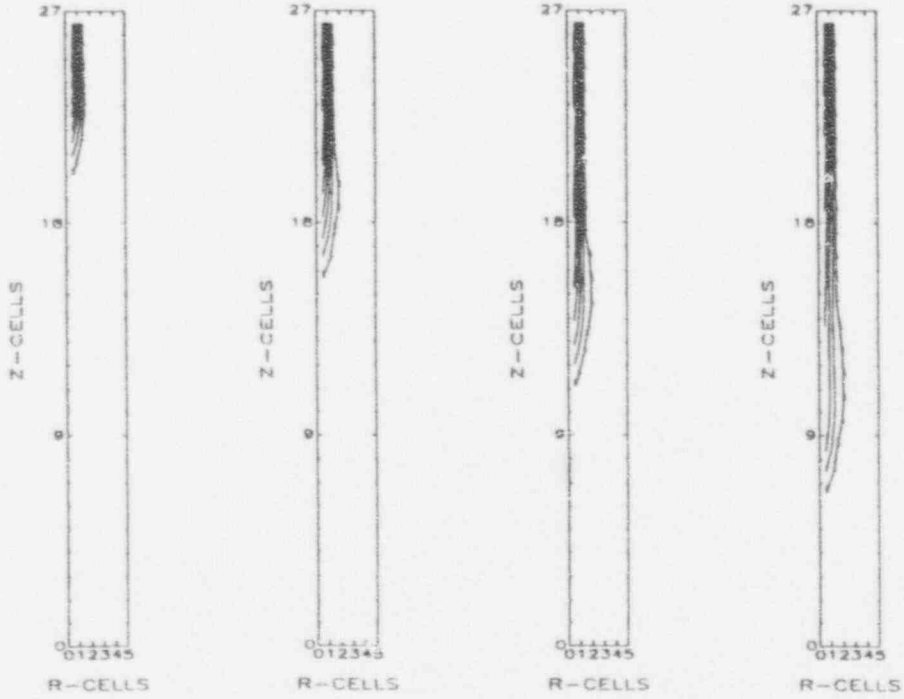

0.25 sec	0.50 sec	0 75 sec	1.00 sec
H=0.2174	H=0.2309	H=0.2270	H=0.2315
L=0.0000	L=0.0000	L=0.0000	L=0.0000

Figure 3.3 (contd)
Outer Instrument Tube Failure–Premixing
Fuel Volume Fraction
(Δr = 3.0 cm, Δz = 20.0 cm)

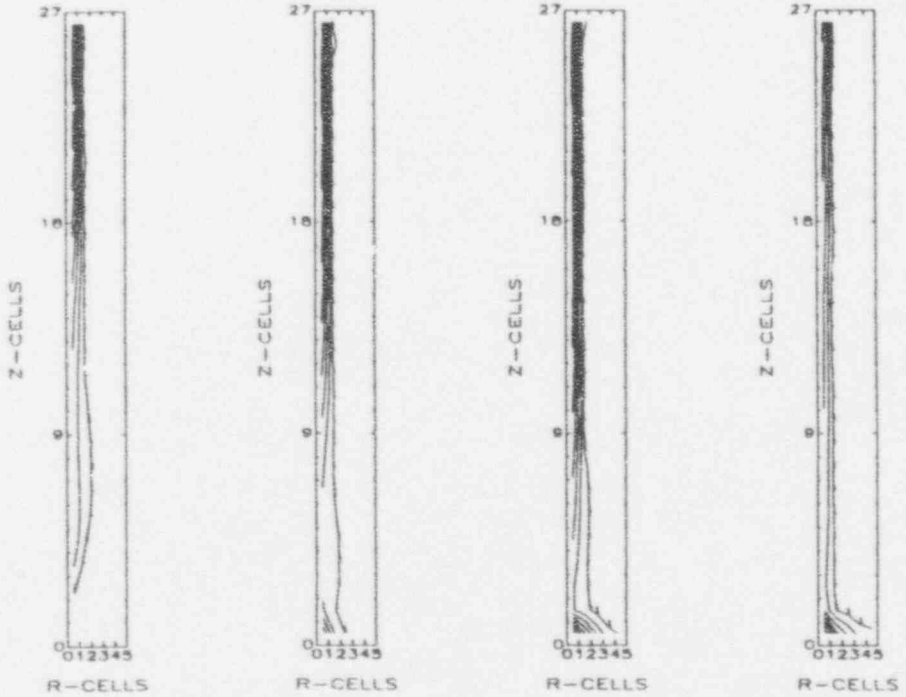

1.25 sec	1.50 sec	1.75 sec	2.00 sec
H=0.2267	H=0.2328	H=0.2269	H=0.3882
L=0.0000	L=0.0000	L=0.0000	L=0.0000

Figure 3.4
Outer Instrument Tube Failure–Premixing
Void Fraction
(Δr = 3.0 cm, Δz = 20.0 cm)

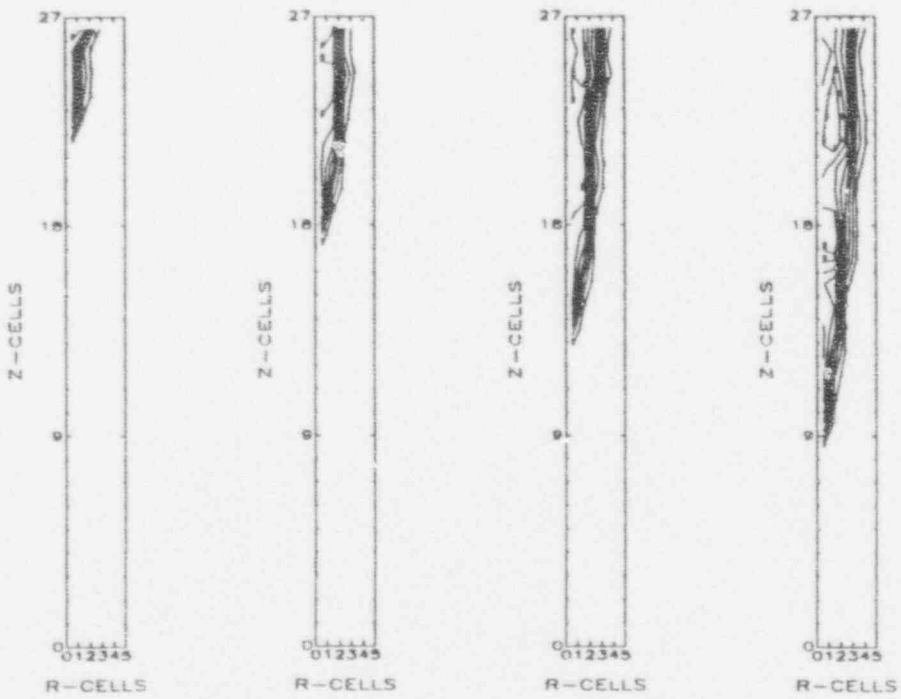

0.25 sec	0.50 sec	0.75 sec	1.00 sec
H=0.7806	H=0.7691	H=0.8567	H=0.9073
L=0.0000	L=0.0000	L=0.0000	L=0.0000

Figure 3.4 (contd)
Outer Instrument Tube Failure–Premixing
Void Fraction
($\Delta r = 3.0$ cm, $\Delta z = 20.0$ cm)

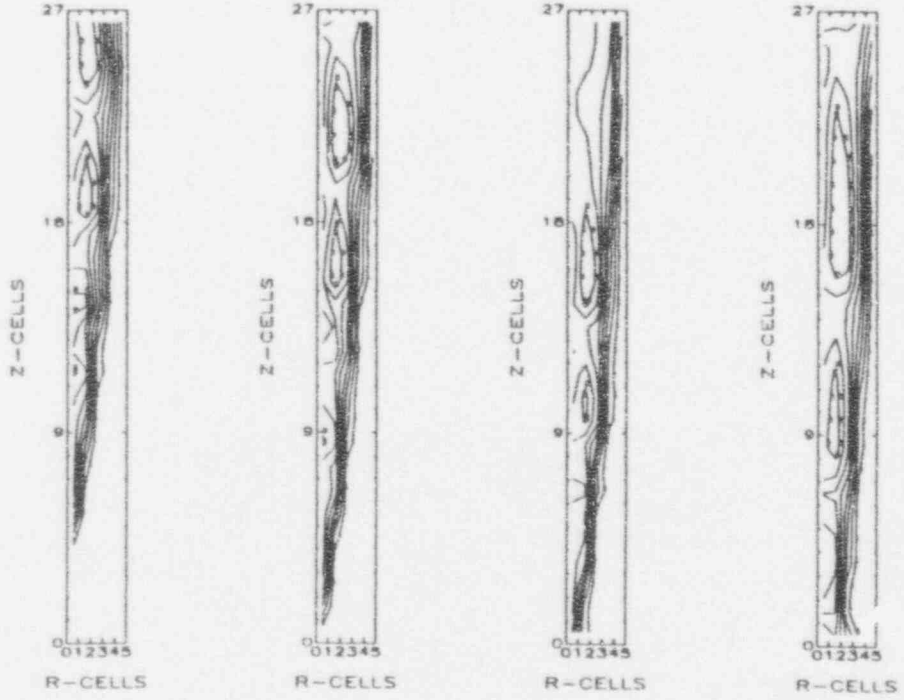

1.25 sec	1.50 sec	1.75 sec	2.00 sec
H=0.9053	H=0.9116	H=0.9341	H=0.9190
L=0.0000	L=0.0000	L=0.0000	L=0.0000

Figure 3.5
Outer Instrument Tube Failure–Premixing
Pressure (bar)
($\Delta r = 3.0$ cm, $\Delta z = 20.0$ cm)

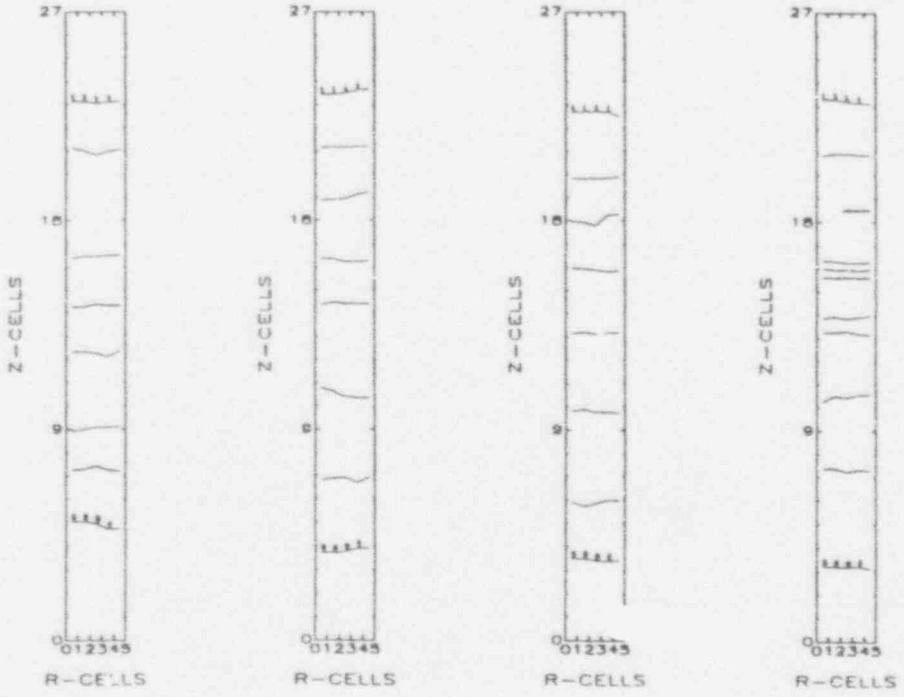

0.25 sec	0.50 sec	0.75 sec	1.00 sec
H=2.425	H=2.527	H=2.576	H=2.537
L=2.011	L=2.004	L=2.020	L=2.034

Figure 3.5 (contd)
Outer Instrument Tube Failure–Premixing
Pressure (bar)
($\Delta r = 3.0$ cm, $\Delta z = 20.0$ cm)

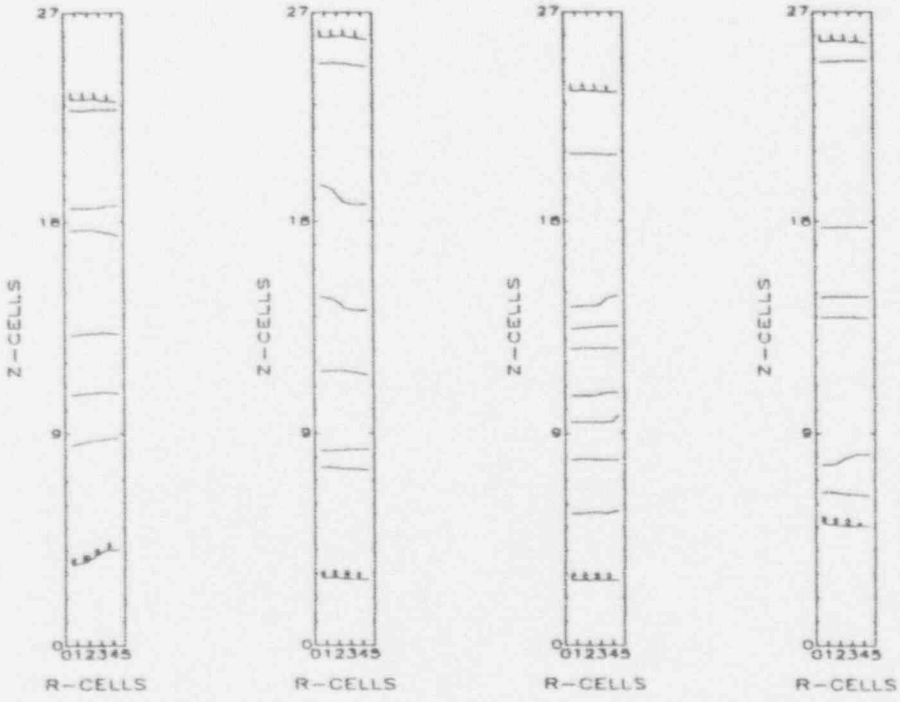

1.25 sec	1.50 sec	1.75 sec	2.00 sec
H=2.466	H=2.506	H=2.484	H=2.434
L=1.982	L=1.979	L=2.008	L=2.008

Figure 3.6
Outer Instrument Tube Failure–Propagation
Fuel Volume Fraction
(Δr = 3.0 cm, Δz = 20.0 cm)

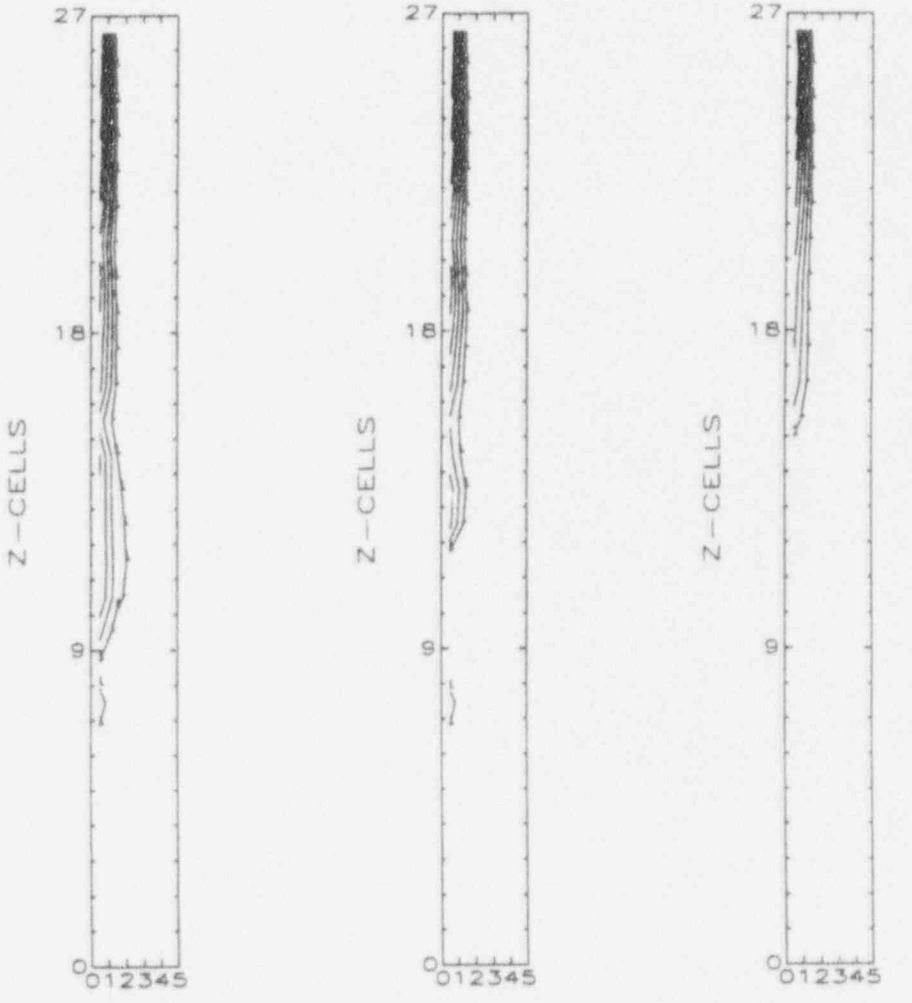

Figure 3.6 (contd)
Outer Instrument Tube Failure–Propagation
Fuel Volume Fraction
(Δr = 3.0 cm, Δz = 20.0 cm)

Figure 3.7
Outer Instrument Tube Failure–Propagation
Void Fraction
($\Delta r = 3.0$ cm, $\Delta z = 20.0$ cm)

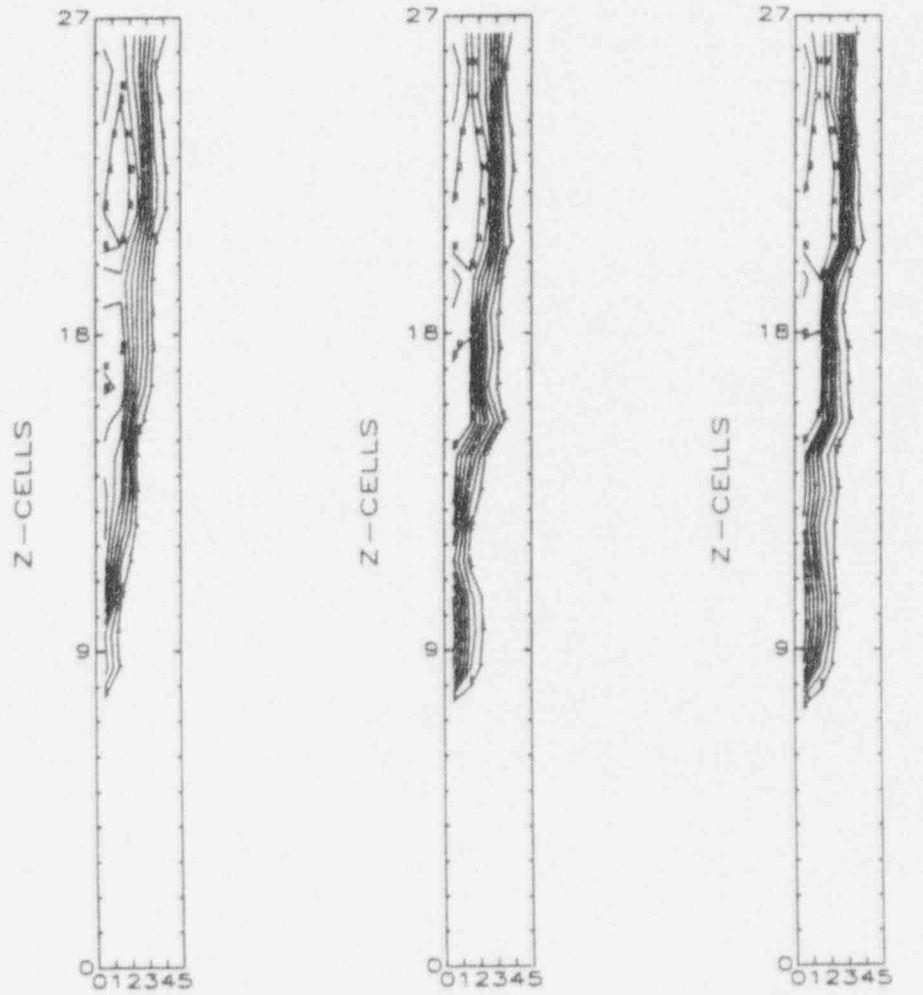

Figure 3.7 (contd)
Outer Instrument Tube Failure–Propagation
Void Fraction
($\Delta r = 3.0$ cm, $\Delta z = 20.0$ cm)

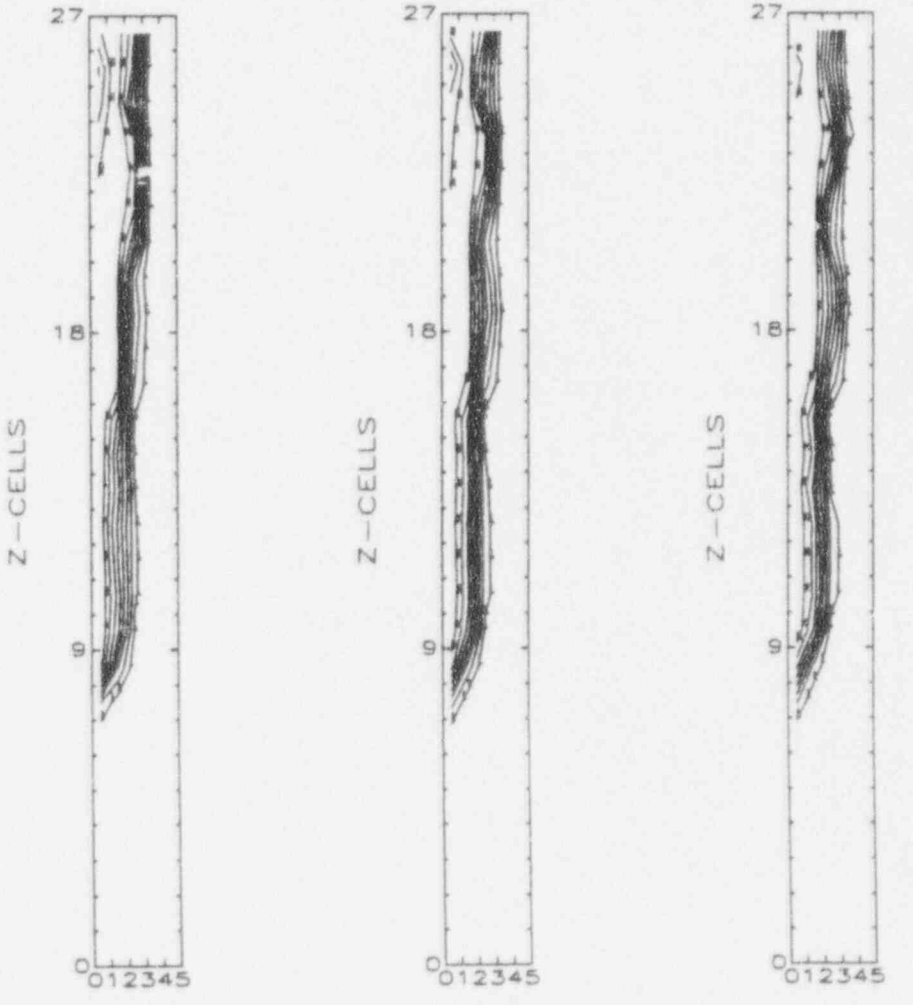

Figure 3.8
Outer Instrument Tube Failure–Propagation
Pressure (bar)
(Δr = 3.0 cm, Δz = 20.0 cm)

2.5 ms
H=14.02
L=2.227

5.0 ms
H=73.47
L=2.746

7.5 ms
H=57.91
L=5.140

Figure 3.8 (contd)
Outer Instrument Tube Failure–Propagation
Pressure (bar)
(Δr = 3.0 cm, Δz = 20.0 cm)

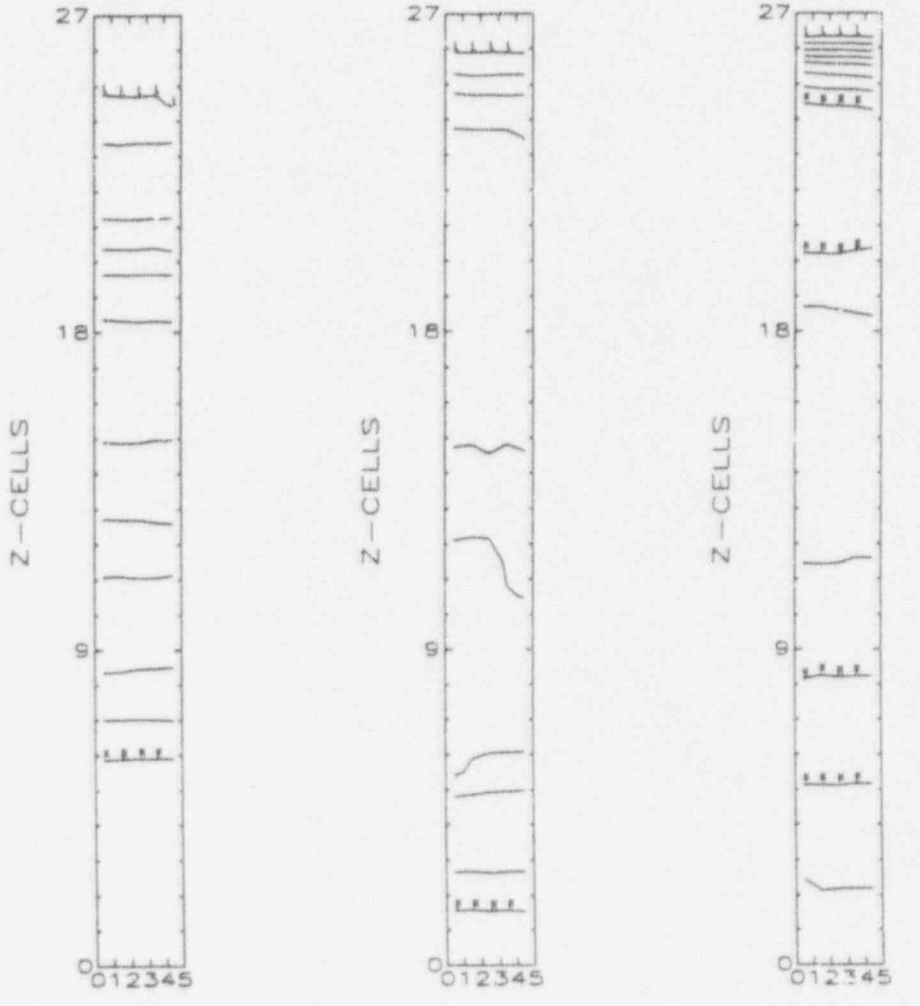

Figure 3.9
Outer Instrument Tube Failure–Propagation
Pressure (bar)
(Δr = 3.0 cm, Δz = 20.0 cm)

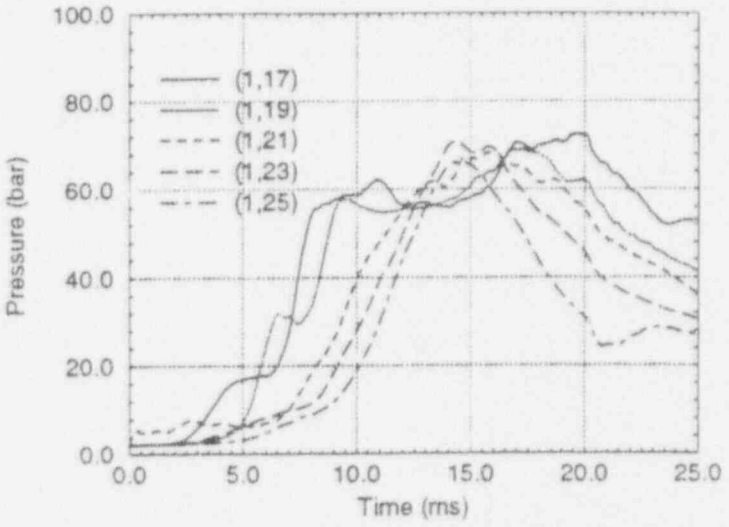

(a) Pressures along melt jet center line

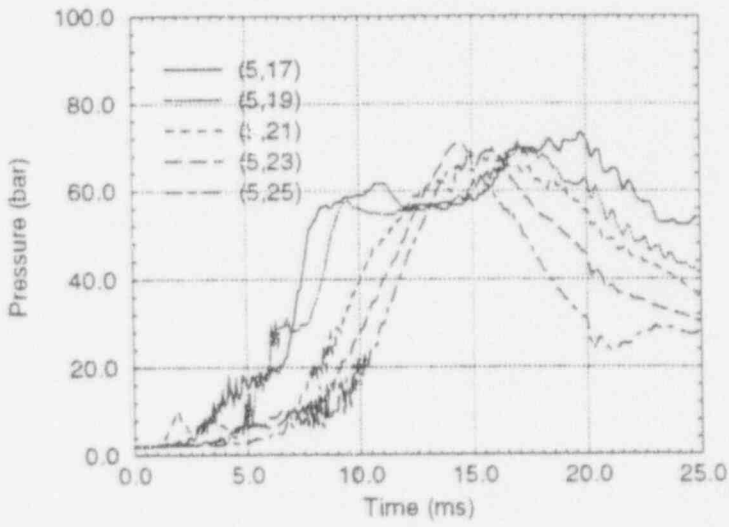

(b) Pressures along corbel support

Figure 3.10
Outer Instrument Tube Failure
Impulse Distribution Along Corbel Support
(Δr = 3.0 cm, Δz = 20.0 cm)

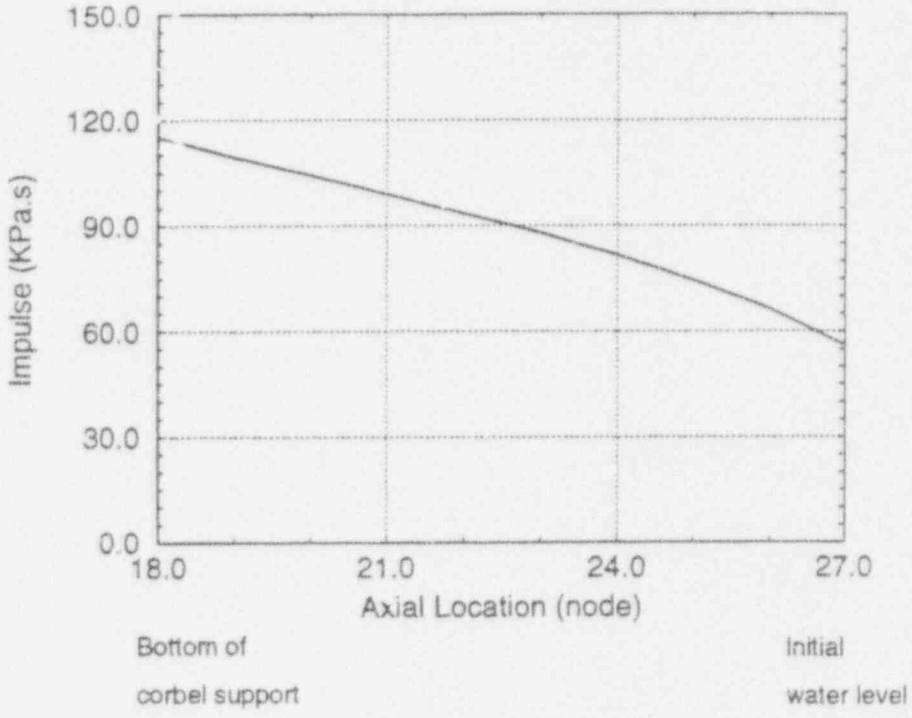

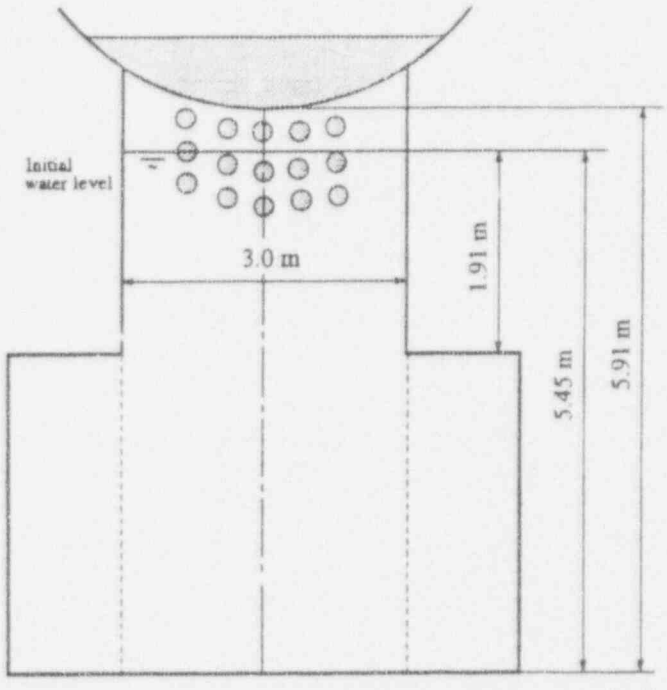

Figure 4.1: Overall Configuration for Multiple Instrument Tube Failures

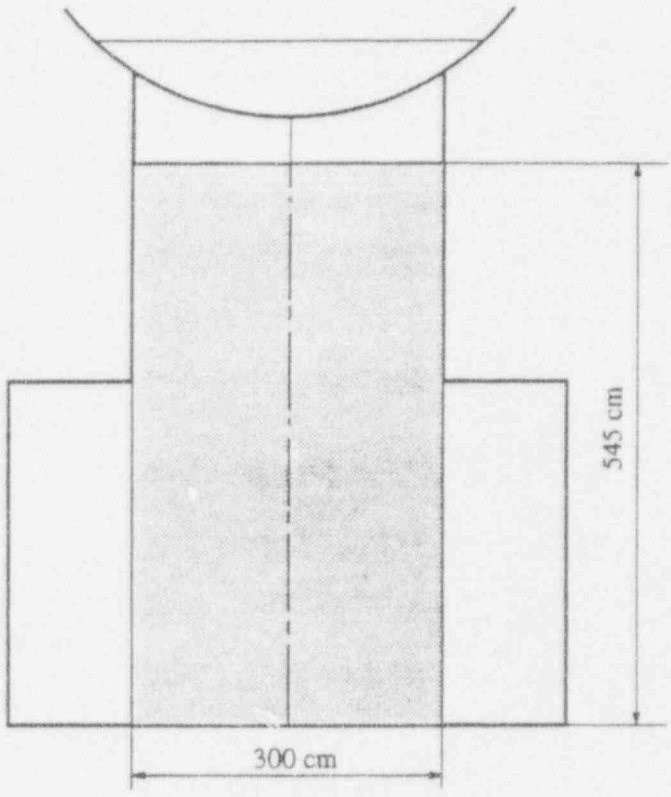

Figure 4.2: Multiple Instrument Tube Failure
(Shaded area represents computational domain
for premixing and propagation calculations)

Figure 4.3
Multiple Instrument Tube Failures–Premixing
Fuel Volume Fraction
(Δr = 15.9 cm, Δz = 20.0 cm)

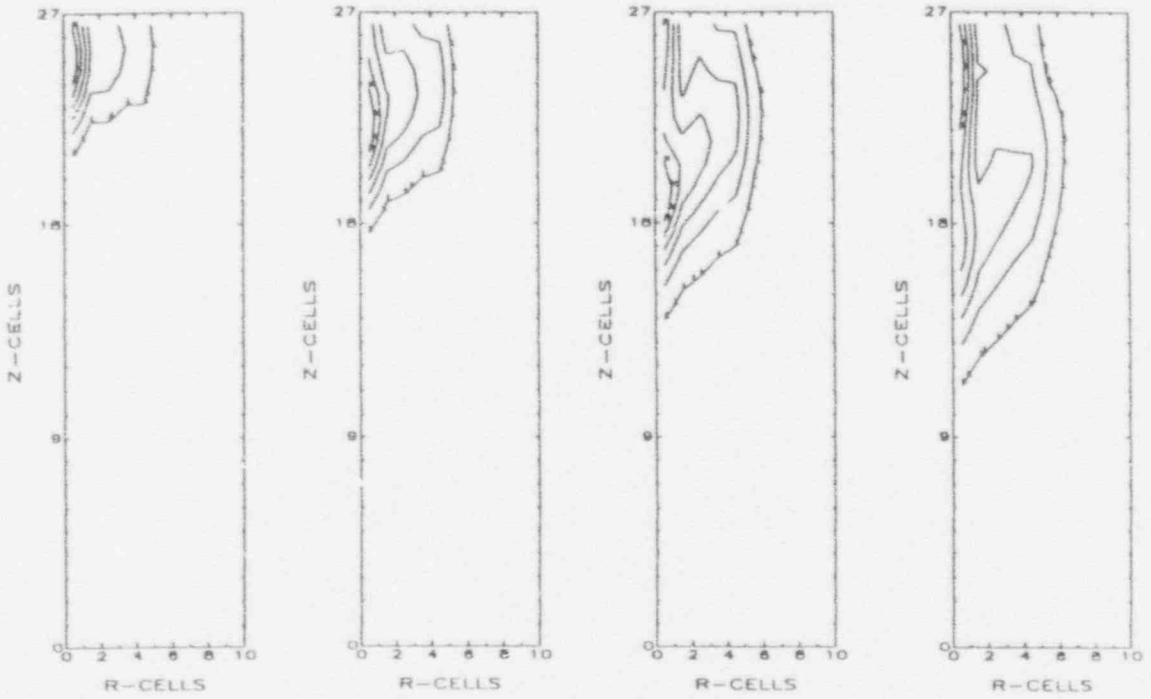

Figure 4.3 (contd)
Multiple Instrument Tube Failures–Premixing
Fuel Volume Fraction
(Δr = 15.0 cm, Δz = 20.0 cm)

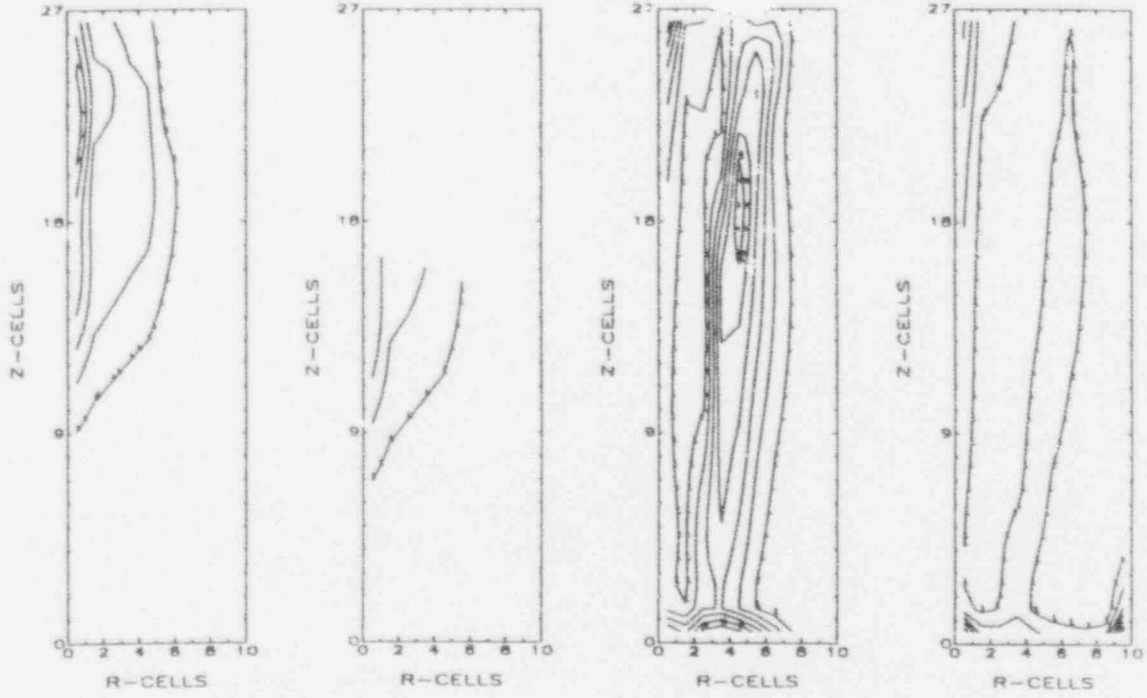

1.25 sec	1.50 sec	1.75 sec	2.00 sec
H=0.0159	H=0.0183	H=0.0071	H=0.0157
L=0.0000	L=0.0000	L=0.0000	L=0.0000

Figure 4.4
Multiple Instrument Tube Failures–Premixing
Void Fraction
(Δr = 15.0 cm, Δz = 20.0 cm)

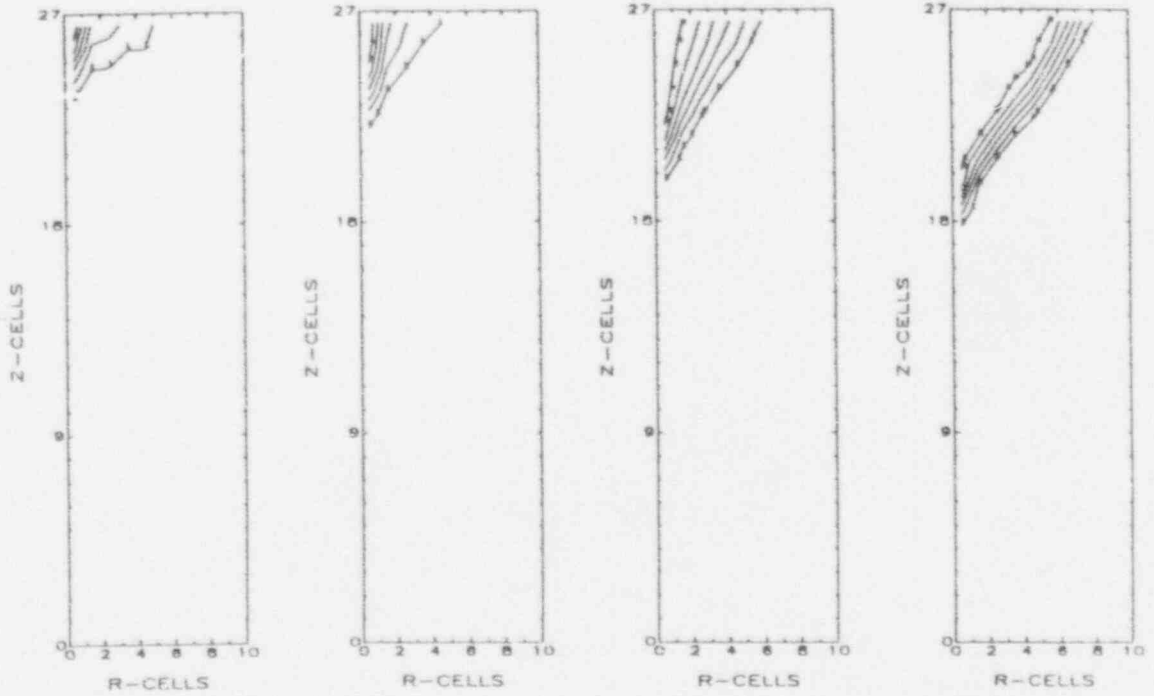

0.25 sec
H=0.0335
L=0.0000

0.50 sec
H=0.2068
L=0.0000

0.75 sec
H=0.6340
L=0.0000

1.00 sec
H=0.7023
L=0.0000

Figure 4.4 (contd)
Multiple Instrument Tube Failures–Premixing
Void Fraction
(Δr = 15.0 cm, Δz = 20.0 cm)

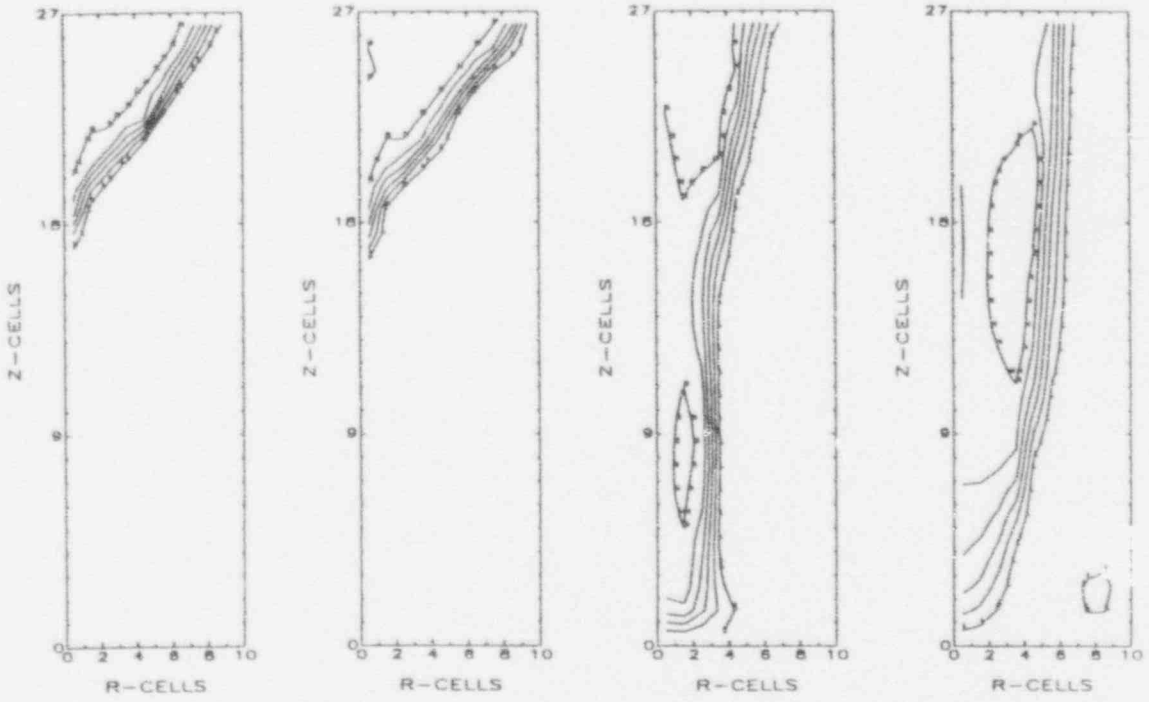

1.25 sec	1.50 sec	1.75 sec	2.00 sec
H=0.7248	H=0.6972	H=0.7643	H=0.8624
L=0.0000	L=0.0000	L=0.0000	L=0.0000

Figure 4.5
Multiple Instrument Tube Failures–Premixing
Pressure (bar)
($\Delta r = 15.0$ cm, $\Delta z = 20.0$ cm)

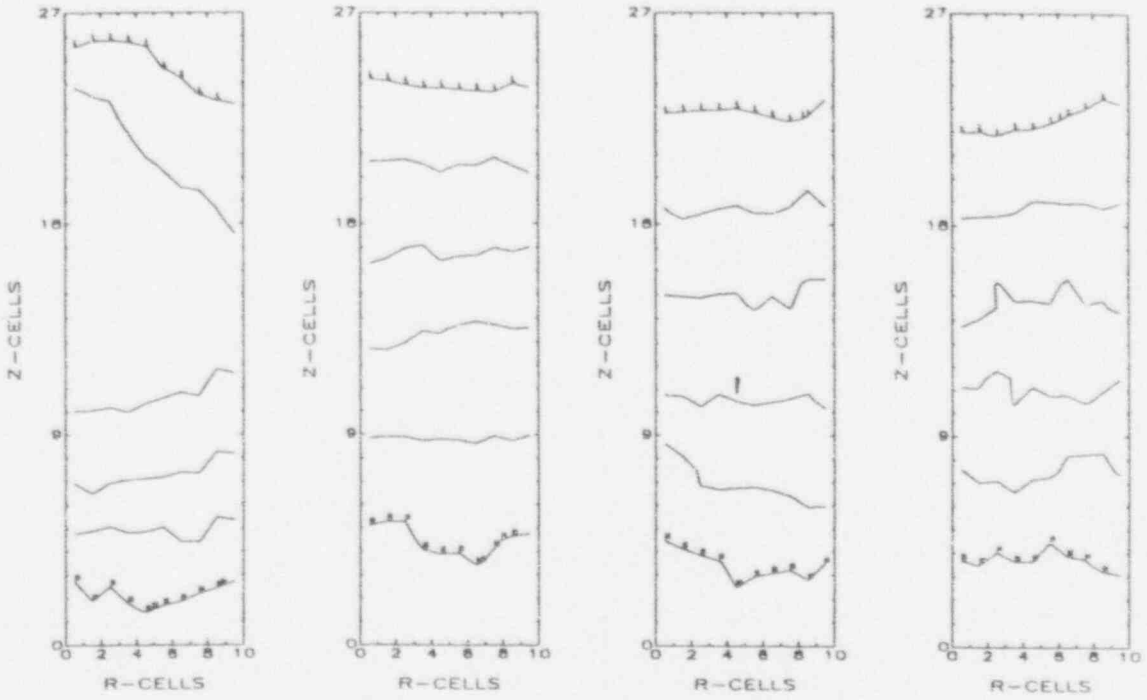

0.25 sec	0.50 sec	0.75 sec	1.00 sec
H=2.366	H=2.736	H=2.586	H=2.469
L=2.018	L=2.033	L=2.022	L=2.012

Figure 4.5 (contd)
Multiple Instrument Tube Failures–Premixing
Pressure (bar)
(Δr = 15.0 cm, Δz = 20.0 cm)

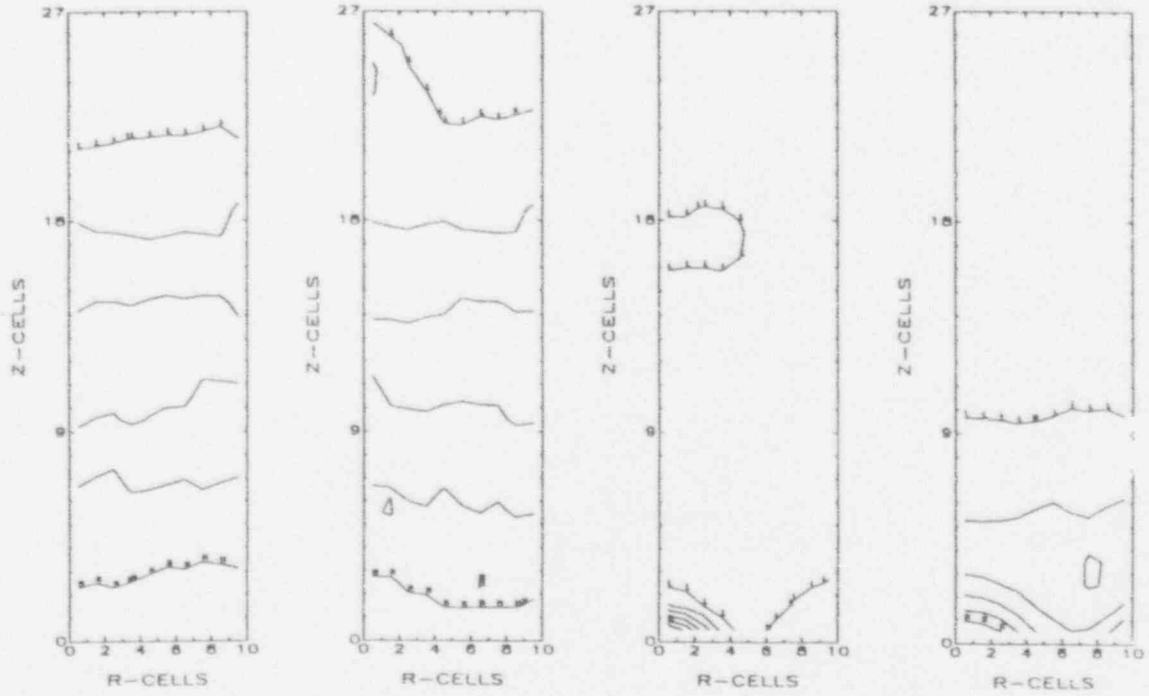

1.25 sec
H=2.519
L=2.009

1.50 sec
H=2.570
L=2.013

1.75 sec
H=4.594
L=2.002

2.00 sec
H=2.925
L=2.019

Figure 4.6
Multiple Instrument Tube Failures–Propagation
Fuel Volume Fraction
(Δr = 15.0 cm, Δz = 20.0 cm)

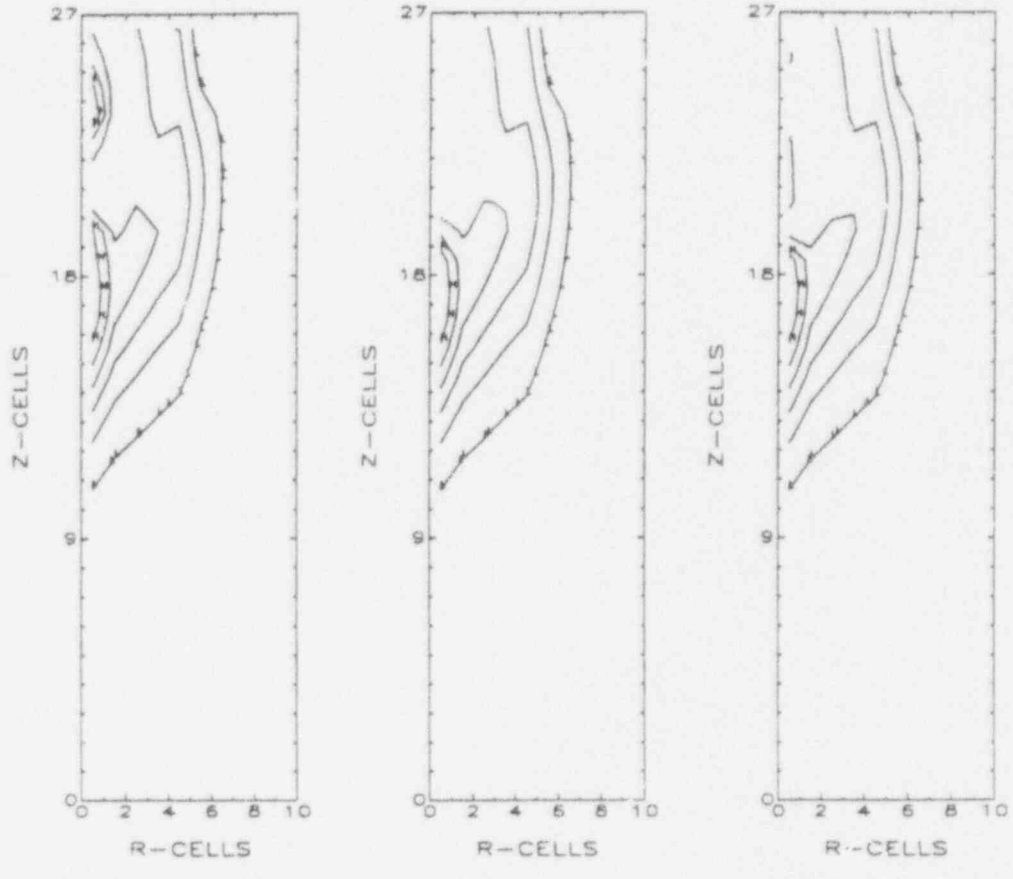

2.5 ms
H=0.0104
L=0.0000

5.0 ms
H=0.0103
L=0.0000

7.5 ms
H=0.0103
L=0.0000

Figure 4.7
Multiple Instrument Tube Failures–Propagation
Void Fraction
(Δr = 15.0 cm, Δz = 20.0 cm)

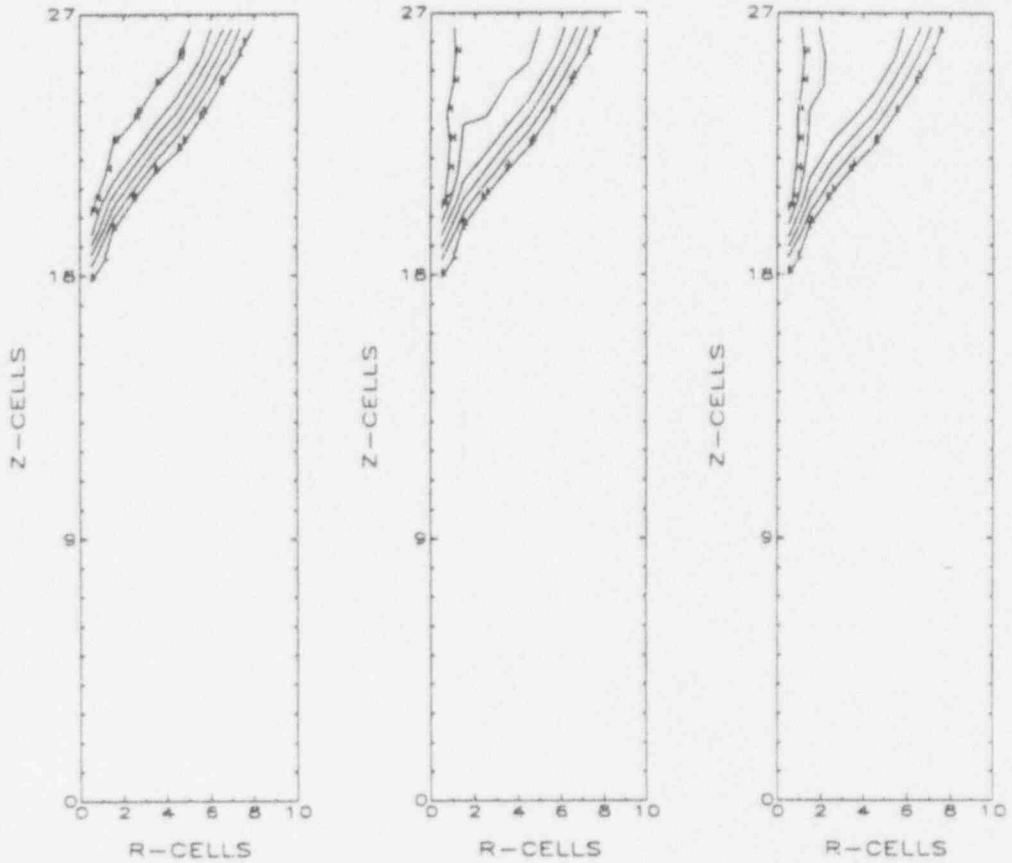

2.5 ms
H=0.7286
L=0.0001

5.0 ms
H=0.8746
L=0.0001

7.5 ms
H=0.9519
L=0.0001

Figure 4.8
Multiple Instrument Tube Failures–Propagation
Pressure (bar)
(Δr = 15.0 cm, Δz = 20.0 cm)

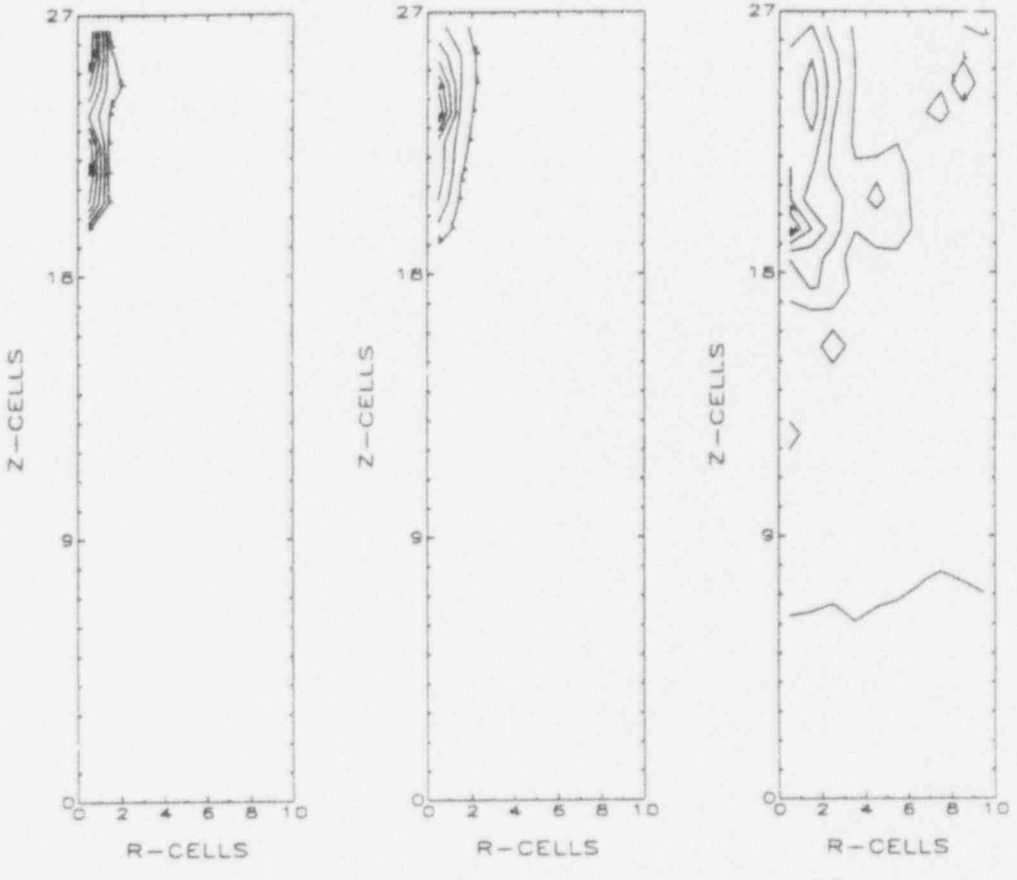

2.5 ms
H=6.966
L=2.029

5.0 ms
H=9.492
L=2.046

7.5 ms
H=5.300
L=1.171

Figure 4.9
Multiple Instrument Tube Failures
Impulse Distribution Along Corbel Support
(Δr = 15.0 cm, Δz = 20.0 cm)

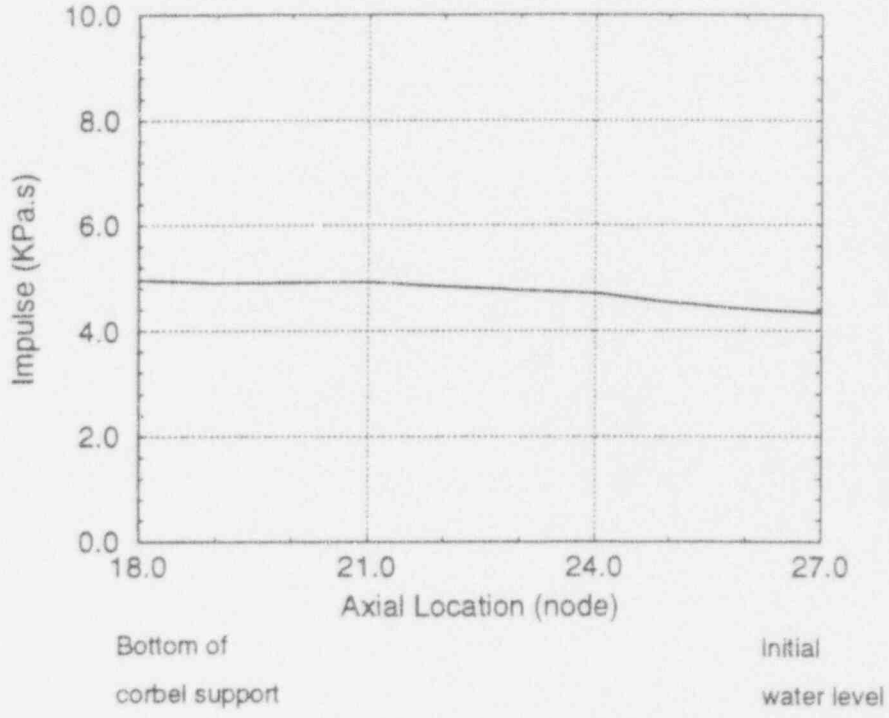

References

[1] W. M. Ren, S. M. Ghiaasiaan, and S. I. Abdel-Khalik, *GT3F: An Implicit Finite-Difference Computer Code for Transient Three-Dimensional Three-Phase Flow Part I: Governing Equations and Solution Scheme*, Numerical Heat Transfer, Part B: Fundamental, Vol. 25, pp. 1-20, 1994.

[2] W. M. Ren, S. M. Ghiaasiaan, and S. I. Abdel-Khalik, *GT3F: An Implicit Finite-Difference Computer Code for Transient Three-Dimensional Three-Phase Flow Part II: Applications*, Numerical Heat Transfer, Part B: Fundamental, Vol. 25, pp. 21-38, 1994.

[3] H. Esmaili and M. Khatib-Rahbar, *Analysis of Ex-vessel Steam Explosions for the Combustion Engineering System 80+*, ERI/NRC 94-201, Energy Research, Inc. March 1994.

[4] R. Clift, J. R. Grace, and M. E. Weber, *Stability of Bubbles in Fluidized Beds*, Ind. Eng. Chem. Fundam, Vol. 13, No. 1, pp. 45-51, 1974.

[5] I. H. Lehrer, *On Bubble and Drop Deformation and Breakup*, Israel J. Technology, Vol. 13, pp. 246-252, 1975.

[6] J. R. Grace, T. Wairegi, and J. Brophy, *Break-up of Drops and Bubbles in Stagnant Media*, Canadian Journal of Chemical Engineering, Vol. 56, pp. 3-8, 1978.

[7] M. Pilch and C. A. Erdman, *Use of Breakup Time Data and Velocity History Data to Predict the Maximum Size of Stable Fragments for Acceleration-Induced*

Breakup of a Liquid Drop, Int. J. Multiphase Flow, Vol. 13, No. 6, pp. 741-757, 1987.

[8] R. Clift, J. R. Grace, and M. E. Weber, *Bubbles, Drops, and Particles*, Academic Press, New York, 1978.

[9] L. P. Hsiang and G. M. Faeth, *Near-Limit Drop Deformation and Secondary Breakup*, Int. J. Multiphase Flow, Vol. 18, No. 5, pp. 635-652, 1992.

[10] D. R. Liles, et al., *TRAC-PF1/MOD1: An Advanced Best Estimate Computer Program for Pressurized Water Reactor Thermal Hydraulic Analysis*, US Nuclear Regulatory Commission Report NUREG/CR-3858, 1986.

[11] P. D. Patel and T. G. Theofanous, *Hydrodynamic Fragmentation of Drops*, J. Fluid Mech., Vol. 103, pp. 207-223, 1980.

[12] N. I. Kolev, *Fragmentation and Coalescence Dynamics in Multiphase Flows*, Experimental Thermal and Fluid Science, Vol. 6, pp. 211-251, 1993.

[13] R. S. Brodkey, *The Phenomena of Fluid Motions*, Addison-Wesley, Reading, Mass., 1967.

[14] M. Baines, *Hydrodynamic Fragmentation in a dense dispersion*, Proc. 4th CSNI Specialists Meeting on Fuel-Coolant Interaction in Nuclear Reactor Safety, Bournemouth, England, 2-5 April, 1979, Vol. 1, pp. 99-111, 1979.

[15] D. S. Kim, M. Bürger, G. Fröhlich, and H. Unger, *Experimental Investigation of Hydrodynamic Fragmentation of Gallium Drops in Water Flows*, Proc. Int.

Meeting on LWR Severe Accident Evaluation, Cambridge, Massachusetts, 28 August - 1 September, Vol. 1, pp. 6.4.1-6.4.7, 1983.

[16] C. Carachalios, M. Burger and H. Unger, *A Transient Two-Phase Model to Describe Thermal Detonations Based on Hydrodynamic Fragmentation*, Proc. Int. Meeting on LWR Severe Accident Evaluation, Cambridge, Massachusetts, 28 August-1 September, 1983.

[17] C. Carachalios, M. Burger and H. Unger, *Triggering and Escalation Behavior of Thermal Detonations*, AIChE Symp. Series, Vol. 81, pp. 259-266, 1985.

[18] W. M. Ren, *Mechanistic Modeling of Steam Explosions*, Ph.D. Dissertation, Georgia Institute of Technology, Atlanta GA, 1994.

[19] M. Bürger, K. Müller, M. Buck, S.-H. Cho, and A. Schatz, *Examination of thermal detonation codes and included fragmentation models by means of triggered propagation experiments in a tin/water mixture*, Nuclear Engineering and Design, Vol. 131, pp. 61-70, 1991.

APPENDICES

A Particle Breakup and Fine Fragmentation Models in $GT3F^{TM}$ Computer Code

A.1 Introduction

Particle breakup is important in the propagation of fast multi-fluid processes, since it determines the interfacial surface area concentrations, and thereby strongly affects the interphase transfer processes. In what follows, recent studies relevant to bubble and droplet breakup and particle fragmentation are reviewed, thereafter the models utilized in the $GT3F^{TM}$ code are presented.

In the forthcoming discussions, distinction is made between hydrodynamic and acceleration-induced breakup mechanisms on the one hand, and shock-induced fine fragmentation on the other. The first governs particulation of liquid or gas phases and breakup of melt droplets during premixing, while the second takes place during the propagation phase of the steam explosions. This distinction is necessary because hydrodynamic and acceleration-induced breakup generate particles typically 1 cm in diameter, whereas shock-induced fragmentation generates fuel particles typically 100 μm in diameter.

A.2 Hydrodynamic and Acceleration-Induced Breakup

A.2.1 Breakup due to Rayleigh-Taylor Instability

When one fluid overlays a less dense fluid, perturbations at the interface tend to grow by Rayleigh-Taylor instability. The breakup of a single bubble or drop rising or falling

freely through stagnant media has thus been attributed to Rayleigh-Taylor instability (Clift et al. [4]). This type of breakup mechanism has been recently studied by Lehrer [5] and Grace et al. [6], who found that the following semi-empirical relation predicts the maximum particle diameter:

$$d^*_{max} = 4\sqrt{\frac{\sigma}{g\Delta\rho}} \tag{1}$$

Grace et al. [6] compared the predicted maximum stable sizes with experimental data of drops and bubbles in viscous liquids for eighteen different systems, and concluded that agreement between the model and experimental results was favorable.

Equation (1) represents the maximum stable particle size; the mean particle size at equilibrium can be obtained from [7]

$$\bar{d} = 2\sqrt{\frac{\sigma}{g\Delta\rho}} \tag{2}$$

A.2.2 Acceleration-Induced Breakup

For acceleration-induced fragmentation, the hydrodynamic stability limit is usually described by the Weber number, which represents the ratio of the disruptive inertia force to the stabilizing surface tension force:

$$We = \frac{\rho_c V_r^2 D}{\sigma} \tag{3}$$

Where ρ_c is the density of the continuous flow field, V_r is the relative velocity between the continuous flow field and the drop or bubble, D is the initial diameter of the drop or bubble, and σ is the surface tension of the particle.

There is a critical Weber number (We_c) below which drop breakup does not occur [8]. For bubbles or low-viscosity liquid drops, this critical Weber number is about 12.

For high-viscosity liquid drops, the viscous effect on breakup has been correlated as [7]:

$$We_c = 12(1 + 1.077On^{1.6}) \tag{4}$$

Where the Ohnesorge number, On, is defined as:

$$On = \frac{\mu_d}{\sqrt{\rho_d D \sigma}} \tag{5}$$

where μ_d is the dynamic viscosity of the drop and ρ_d is the density of the drop. According to Eq. (4), the drop breakup at high Ohnesorge numbers is progressively more difficult. Experiments performed recently by Hsiang and Faeth show [9] show that there is no drop fragmentation for $On > 4$.

When $We > We_c$ for a particle, acceleration induced fragmentation takes place. Fragmentation continues over a break-up time, t_b, which represents the time period after which the bubble or drop and its fragments no longer undergo fragmentation. Acceleration induced fragmentation can occur due to several different mechanisms. According to Pitch and Erdman [7], these mechanisms and their boundaries are:

- Vibrational breakup — $We \leq 12$
- Bag breakup — $12 < We \leq 50$
- Bag-and-stamen breakup — $50 < We \leq 100$
- Sheet stripping — $100 < We \leq 350$
- Wave crest stripping followed by catastrophic breakup — $We > 350$

The aforementioned authors also correlated the total breakup time, t_b, based on the published experimental data from eight sources for liquid drops falling in gases, according to [7]:

$$
\begin{aligned}
T_b &= 6(We-12)^{-0.25} && 12 \le We \le 18 \\
T_b &= 2.45(We-12)^{0.25} && 18 \le We \le 45 \\
T_b &= 1.41(We-12)^{0.25} && 45 \le We \le 351 \\
T_b &= 0.766(We-12)^{0.25} && 351 \le We \le 2670 \\
T_b &= 5.5 && We \ge 2670
\end{aligned}
$$

Where the dimensionless breakup time, T_b, is defined as:

$$T_b = t_b \frac{V_r}{D} \epsilon_c^{0.5} \tag{6}$$

where

$$\epsilon_c = \sqrt{\rho_c / \rho_d} \tag{7}$$

For the liquid-liquid systems, based on limited experimental data, Pilch et al. [7] suggested that the breakup time is comparable to that of the gas-liquid systems.

The conventional way to estimate the maximum stable diameter due to acceleration-induced breakup is to write:

$$d^*_{max} = We_c \frac{\sigma}{\rho V_r^2} \tag{8}$$

However, the predicted fragment sizes from Eq. (8) are reported to be too small by nearly two orders of magnitude [7], and may cause numerical difficulties [10]. Pilch et al. [7] studied the experimental observations, and pointed out that the aforementioned conventional estimate of the maximum stable diameter fails primarily because of the erroneous assumption that fragment Weber numbers decrease only because fragment

sizes decrease. They introduced a new way to estimate the maximum stable particle diameter, in which the change of the relative velocity before and after the breakup is accounted for. Thus,

$$d^*_{max} = We_c \frac{\sigma}{\rho V_r^2} \left(1 - \frac{V_d}{V_r}\right)^{-2} \tag{9}$$

where V_d is the velocity of the fragment cloud when all breakup processes cease.

Pilch et al. compared the modified maximum stable diameter with experimental data [7]. The results show that the correlation represented by Eq. (9) is valid for $350 < We < 10^5$. However, for $We \leq 350$, the correlation over predicts the fragment sizes. The authors also pointed out that the maximum fragment size is about twice as large as the mass median fragment size, and that ratio is independent of the Weber number [7].

Correlations for estimating the fragment cloud velocity V_d are now discussed. For the gas-liquid (liquid drops falling in gases) systems, Pilch [7] recommended the following empirical correlation:

$$\frac{V_d}{V_r \epsilon^{0.5}} = \frac{3}{4} C_d T_b + 3BT_b^2 \tag{10}$$

Here, C_d is the drag coefficient for a rigid constant-mass sphere, and B is an empirical constant given by:

$$C_d = 1 \qquad B = 0.116 \qquad \text{(compressible flow)} \tag{11}$$

$$C_d = 0.5 \qquad B = 0.0758 \qquad \text{(incompressible flow)} \tag{12}$$

For the liquid-liquid systems, the following correlations can be used [7]:

$$\frac{V_d}{V_r \epsilon^{0.5}} = \frac{\frac{3}{4} C_d T_b}{1 + \frac{3}{4} C_d \epsilon^{0.5} T_b} \tag{13}$$

And C_d is suggested to be 2.5 to 3.0 based on the measurements of Patel and Theofanous [11] for a mercury-water system.

The available experimental data for breakup of gas bubbles in liquid systems are limited. Kolev [12] suggested estimating V_d by Kutateladze's terminal velocity. Accordingly,

$$V_r - V_d = \sqrt{2}\left[\frac{\sigma g \Delta\rho}{\rho^2}\right]^{1/4} \tag{14}$$

Substituting Eq. (14) into Eq. (9), one obtains the upper limit of the bubble size in the flow,

$$d^*_{max} = \frac{1}{2} We_c \sqrt{\frac{\sigma}{g\Delta\rho}} \tag{15}$$

A lower limit can also be specified for particles resulting from acceleration-induced fragmentation. Brodkey [13] showed that bubbles with a diameter smaller than $\frac{1}{2}(2.53)\sqrt{\frac{\sigma}{g\Delta\rho}}$ behave as solid spheres and are not subject to further splitting. Therefore, the stable bubble size range after fragmentation should be,

$$\frac{1}{2}(2.53)\sqrt{\frac{\sigma}{g\Delta\rho}} \leq d^* < \frac{1}{2} We_c \sqrt{\frac{\sigma}{g\Delta\rho}} \tag{16}$$

A.2.3 Shock-Induced Fine Fragmentation

Fragmentation of the molten fuel during the propagation phase of steam explosions generates tiny debris, typically 50 - 100 μm in diameter. Owing to the small debris size, the fragmented debris is assumed to reach thermodynamic equilibration with the liquid coolant instantaneously. Adequate modeling of this fine fragmentation rate is crucial in steam explosion modeling.

Various fragmentation mechanisms have been proposed in recent years. Hydrodynamic fragmentation models which appear to be better developed and validated at

this time, are used in our model development. In hydrodynamic models, the forces responsible for fragmentations are directly related to the relative velocity between the fluids.

The hydrodynamic fragmentation phenomena in steam explosions have been experimentally investigated by several authors. Patel and Theofanous [11] studied the fragmentation of mercury, gallium and acetylene tetrabromide drops in water, using a shock tube to produce a pressure pulse in order to initiate fragmentation. They found that there was no Bond number (which represents the ratio of accelerational forces to surface tension forces) threshold for the onset of fragmentation. They postulated that Rayleigh-Taylor instability was the dominant mechanism for fragmentation process, and suggested a dimensionless breakup time of about 0.4, which is much shorter than those observed in other experiments.

In contrast to the Patel and Theofanous' investigations, Baines [14] found that both capillary wave growth and boundary-layer stripping contributed to fragmentation. For Weber numbers in the range of 100-2000, the stripping process was found to be dominant and the breakup time was approximately constant and given by:

$$T_b \sim 4.0 \tag{17}$$

Kim et al. [15] studied the hydrodynamic fragmentation of gallium drops in water for Weber numbers in the range of 30-3519. They observed a gradual increase in the efficiency of boundary layer stripping as the Weber number was increased, and reported the following observations. At a Weber number of 30, the gallium drops broke into two droplets; for $100 < We < 500$, a closed, thin gallium skin was removed from the drop and finally broke into smaller fragments; in the range of Weber numbers

500 - 1300, direct stripping of fragments was observed parallel to the draw-off of closed skins, and finally, for $1300 < We < 3600$, direct boundary layer stripping effect was dominant. The dimensionless breakup time was found to be in the range of 3.5 - 6.6, with no clear dependence on the Weber number.

Carachalios et al. [16, 17] studied the experimental data of Kim et al. [15], and produced a dynamic fragmentation model. In their model, the rate of mass loss of a single fuel particle due to boundary layer stripping is given by:

$$\frac{dm}{dt} = C_{frag} V_r \pi D_d^2 \sqrt{\rho_c \rho_d} \tag{18}$$

Where $C_{frag} \sim 1/6$.

A.2.4 Breakup Models in $GT3F^{TM}$

In modeling the particulation of gas or liquid phases, and the breakup of the fuel melt, hydrodynamic and acceleration-induced breakup mechanisms are both considered. The bubble and droplet diameters are flow regime dependent, and are discussed in detail in [18]. The melt average particle size is found from:

$$D_3 = min\left\{2\sqrt{\frac{\sigma}{g \mid \rho_3 - rho_c \mid}} \ , \ \frac{1}{2} We_c \frac{\sigma}{\rho_c (V_{r,c} - V_d)^2}\right\} \tag{19}$$

where ρ_c and $V_{r,c}$ are the average coolant density and the relative velocity between the melt particle and coolant, respectively, and are calculated as follows:

$$\rho_c = \alpha' \rho_1 + (1 - \alpha_1)\rho_2 \tag{20}$$

$$V_{r,c} = fraco\alpha' \rho_1 \vec{U}_1 + (1 - \alpha_1)\rho_2 \vec{U}_2 \rho_c - \vec{U}_3 \tag{21}$$

In the above equations, subscripts 1, 2, and 3 represent the gas, liquid coolant, and melt phases, respectively, and

$$\alpha' = \frac{\alpha_1}{\alpha_1 + \alpha_2} \tag{22}$$

where α_k represents the volume fraction of phase k in the three-phase mixture. Furthermore, during the premixing phase, we assume

$$D_3 \geq 1cm \tag{23}$$

The latter limit is imposed based on the model validation with experimental data, which indicate that the imposition of the above lower limit results in good prediction of the transient progression during the propagation and expansion phases.

Shock-induced fine fragmentation is assumed to start when for the unfragmented melt droplets

$$We > We_c^* \tag{24}$$

where We_c^* is an empirically adjusted critical Weber number. Parametric and sensitivity calculations, to be explained later, indicate that good agreement between the model and the data from the KROTOS-21 test [19] is obtained by assuming $We_c^* = 100$.

Following the initiation of shock-induced fine fragmentation, stripping of the molten fuel during the propagation phase is modeled using the above described model of Carachalios [16], represented by Eq. (18). Thus, assuming the melt particles remain spherical during boundary layer stripping, the rate of fragmentation, per unit mixture volume, J_{32}, is calculated from:

$$J_{32} = \alpha_3 |\vec{U}_c - \vec{U}_3| \sqrt{\rho_c \rho_3} / D_3 \tag{25}$$

where D_3 is the fuel particle diameter before fragmentation, and $\vec{U}_c$ and ρ_c are the coolant effective velocity and density, respectively. When $\alpha_1' < 0.2$, it is assumed that all the fuel particles are surrounded by, and hydrodynamically interact with, the liquid coolant only. Thus,

$$\vec{U}_c = \vec{U}_2 \tag{26}$$

$$\rho_c = \rho_2 \tag{27}$$

However, when $\alpha_1' \geq 0.2$, it is assumed that the fuel particles hydrodynamically interact with both gas and liquid. Then, $\vec{U}_c$ and ρ_c are calculated from:

$$\vec{U}_c = \frac{\alpha_1'\rho_1\vec{U}_1 + (1-\alpha_1')\rho_2\vec{U}_2}{\alpha_1'\rho_1 + (1-\alpha_1')\rho_2} \tag{28}$$

where ρ_c is found from Eq. (20).

The stripped fuel is fragmented into tiny particles, typically $\approx$ 10 - 100 μm in diameter. Owing to the small debris size, the fragmented debris is assumed to reach thermodynamic equilibrium with the liquid coolant instantaneously. Estimation of the fine debris size is thus not needed.

B Simulation of KROTOS-21 Steam Explosion Experiment

$GT3F^{TM}$ was used to simulate the KROTOS Test # 21 [19], whereby the fragmentation model in the code was empirically adjusted to provide the best agreement with the experimentally-measured pressure histories. The simulation encompasses premixing and the subsequent propagation phases of the explosion. The simulation results are described in this appendix.

In this experiment molten tin, initially at 1350 K temperature, was poured into water at 360 K temperature. The water level height above the bottom of the test section was 1.1 m, and the pressure was 1 bar. Triggering took place about 1.05 s after molten tin arrived at the water level, at which time about 6.5 kg of tin had already mixed with the water. Figure B-1 depicts the test section.

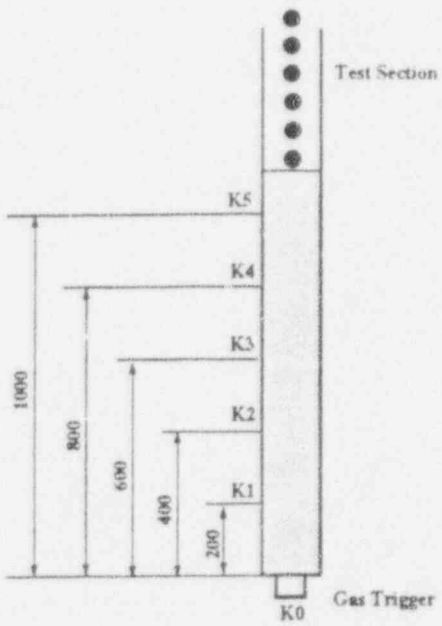

Figure B.1: Schematic and nodalization of KROTOS steam explosion experiments (all dimensions in mm).

B.1 Premixing

The water-filled portion of the test section was represented by 11 axial nodes, each 10 cm in length. $GT3F^{TM}$ simulation of the premixing phase of the steam explosion test starts from the instant molten tin entered water, and continues for 1.05 s, at which time triggering is imposed. Based on experimental observations and hand calculations, it is assumed that the molten tin particles, upon arriving at the water

level, had a velocity of 2.5 m/s, and a diameter of 2.5 cm. The boundary condition at $z = 1.1$ m, representing the water level, was thus set as:

$$P = 1 \text{ bar}$$
$$v_3 = -2 \text{ m/s}$$
$$T_3 = 1350 \text{ K}$$
$$\alpha_3 = 0.069$$

where the quantities v_3, T_3, and α_3 represent velocity, temperature, and volume fraction of the melt fluid at the boundary, respectively.

The melt particle diameters, as described in Section A.2 of Appendix A, are determined by applying hydrodynamic and acceleration-induced breakup models. In addition, a lower limit for the melt particle diameter can also be imposed. In what follows, simulation results will be presented for $DP = 1$ cm and $DP = 0.5$ cm as the lower limits for melt particle diameter.

Figures B2-a, B2-b, and B2-c represent the predicted pressure, void fraction, and melt volume fraction profiles in the test section, respectively.

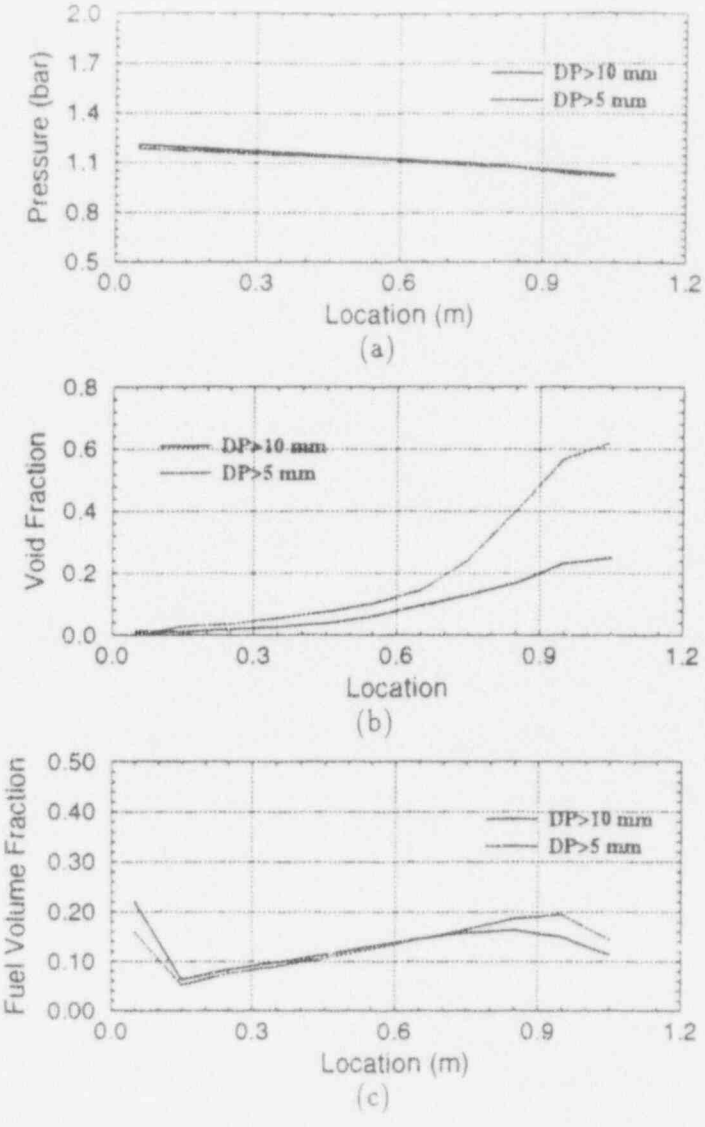

Figure B.2: Premixing predictions for KROTOS-21. (a) Pressure; (b) Void fraction; (c) Fuel Volume Fraction.

As noted in Figure B2-a, the pressure profiles are relatively flat, and the slight pressure gradients are due to hydrostatic head. The void fraction profiles depicted in

Figure B2-b indicate that the void fraction distribution is more uniform for $DP = 1$ cm. Near the top of the water pool the void fraction is high mainly due to the longer exposure time to the hot melt, and partially due to the upward migration of bubbles generated deeper in the pool. The fuel volume fraction profiles in Figure B2-c show only a slight difference between calculation results for $DP = 1$ cm and $DP = 0.5$ cm. Upon entering the water, the velocity of melt particles is reduced due to higher drag, and as a result a slight increase of melt volume fraction with water depth can be noted near the pool surface. Also, as noted, when the melt particles reach the bottom of the pool they accumulate in the lowest node.

As noted, the results obtained with a melt particle diameter lower limit of $DP = 0.5$ cm showed a strongly nonuniform void fraction distribution in the pool at the end of the premixing. This resulted in pressure histories during the propagation phase which were in complete disagreement with the experimental observations. Consequently, all the calculations in this document were carried out using $DP = 1.0$ cm a the lower limit on melt particle diameter during premixing.

B.2 Propagation

The predicted test section parameters at the end of the premixing phase were used as the initial condition for the propagation phase, as described below.

The test section was renodalized, and 5-cm axial nodes were used for more accurate simulation.

The explosion was triggered in the experiment by mechanical destruction of a membrane at the bottom of the test section, which separated the test section from a

15 cm^3 gas volume, initially at 12 MFa pressure. This was simulated in the computer model by imposing a gas flux boundary condition, where gas at the velocity of sound (210 m/s) flowed into the test section for a period of 10 micro second.

Calculated pressure histories at locations K1 through K5 are compared with the reported experimental results [19] in Figure B3. The fragmentation model in $GT3F^{TM}$ uses a melt particle critical Weber number, We_c^*. Fragmentation takes place only when $We > We_c^*$ for the melt particles (See Section A.3 in Appendix A). This critical Weber number will be empirically adjusted here in order to obtain the best possible agreement between model-predicted and experimentally-measured pressure histories.

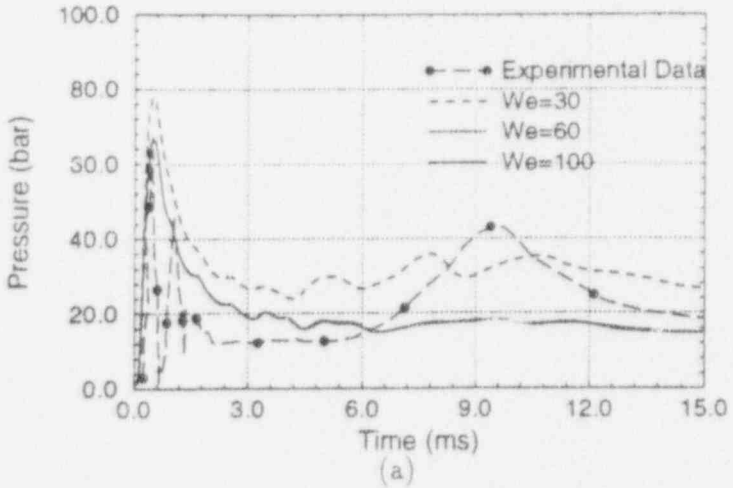
Experimental Data
We=30
We=60
We=100
Pressure (bar)
Time (ms)
100.0
80.0
30.0
40.0
20.0
0.0
0.0
3.0
6.0
9.0
12.0
15.0

(a)

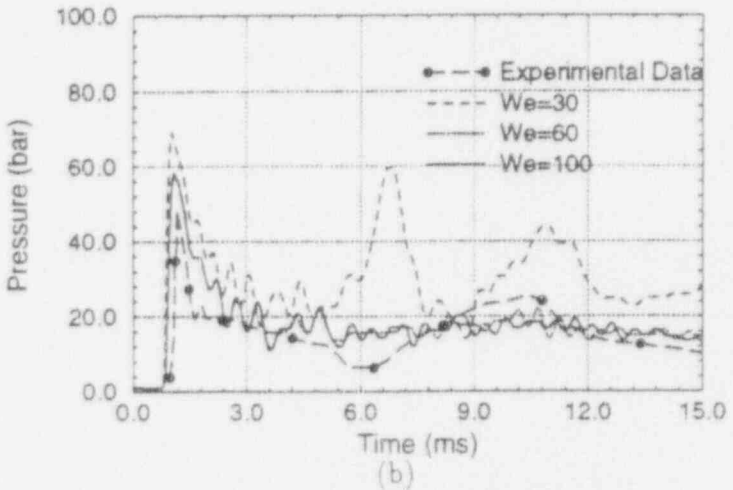
Experimental Data
We=30
We=60
We=100
Pressure (bar)
Time (ms)
100.0
80.0
60.0
40.0
20.0
0.0
0.0
3.0
6.0
9.0
12.0
15.0

(b)

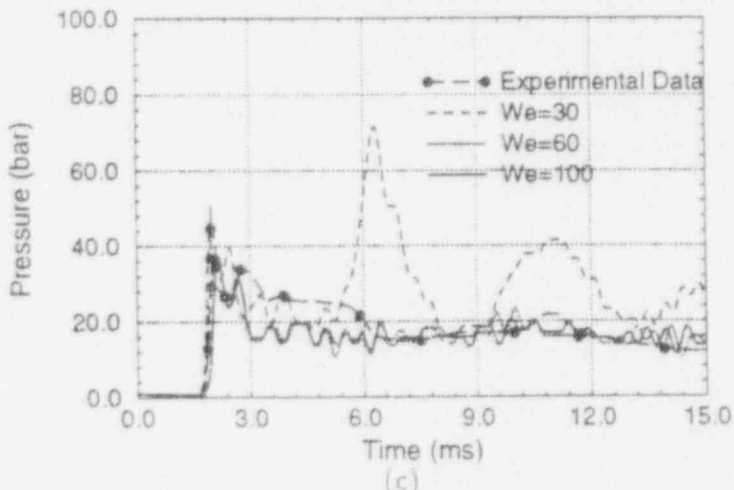
Experimental Data
We=30
We=60
We=100
Pressure (bar)
Time (ms)
100.0
80.0
60.0
40.0
20.0
0.0
0.0
3.0
6.0
9.0
12.0
15.0

(c)